PETROLOGICAL AND GEOPHYSICAL INVESTIGATIONS OF MAFIC ROCK PROPERTIES IN THE SNAKE RIVER PLAIN, IN THE MOSCOW-PULLMAN AQUIFER, AND IN LUNAR IMPACT CRATERS

A Dissertation

Presented in Partial Fulfillment of the Requirements for the

Degree of Doctor of Philosophy

with a

Major in Geology

in the

College of Graduate Studies

University of Idaho

by

Mark W. Piersol

Major Professor: Kenneth F. Sprenke, Ph.D.

Committee Members: Leslie L. Baker, Ph.D.; Thomas Williams, Ph.D.; Owen K. Neill, Ph.D.

Department Administrator: Mickey E. Gunter, Ph.D.

May 2016

Authorization to Submit Dissertation

This dissertation of Mark W. Piersol, submitted for the degree of Doctor of Philosophy with a Major in Geology and titled “PETROLOGICAL AND GEOPHYSICAL INVESTIGATIONS OF MAFIC ROCK PROPERTIES IN THE SNAKE RIVER PLAIN, IN THE MOSCOW-PULLMAN AQUIFER, AND IN LUNAR IMPACT CRATERS," has been reviewed in final form. Permission, as indicated by the signatures and dates below, is now granted to submit final copies to the College of Graduate Studies for approval.

Major Professor:	_____	Date:	_____
	Kenneth F. Sprenke, Ph.D.		
Committee Members:	_____	Date:	_____
	Leslie L. Baker, Ph.D.		
	_____	Date:	_____
	Thomas Williams, Ph.D.		
	_____	Date:	_____
	Owen K. Neill, Ph.D.		
Department Administrator:	_____	Date:	_____
	Mickey E. Gunter, Ph.D.		

Abstract

This dissertation is composed of three separate papers presented in three chapters. Although largely unrelated, the three papers all deal with mafic igneous rock. Chapter 1 is an investigation into the petrological properties of basalts found in the western and eastern Snake River plain of Idaho and the Saddle Mountain basalts of Washington and Idaho. Many of these basalts, separated by up to 600 km and spanning a period of over 12 Ma, appear to have been produced by a common mantle source. A tectonic model is proposed to explain their common origins. This paper was submitted to the journal Geosphere with co-author Professor Dennis J. Geist. Chapter 2 describes a geophysical model of the Kamiak Gap located in the basalt-hosted Moscow-Pullman aquifer of Idaho and Washington. Contrary to previous models, we conclude that there is indeed a hydrological connection between the southern and northern sections of the aquifer through the Kamiak Gap. This chapter is shown on the Palouse Basin Aquifer Committee Website http://www.webpages.uidaho.edu/pbac) and contributed, in part, to the publication of a separate hydrology oriented paper in the journal *Resources* (Piersol and Sprenke, 2015). Chapter 3 presents a geomorphometric model of impact craters on the Lunar highlands that is used in conjunction with published GRAIL Bouguer reduction density and residual Bouguer anomaly results to model the average bulk density of the mafic megaregolithic crust of the Moon. The currently visible craters in the lunar highlands are shown to have negative mass deficiencies, which correlate with elevation. The bulk density of the lunar megaregolith crust is found to be much lower than the generally used value found by minimizing the correlation between gravity and topography. This research has been published in part in a Lunar and Planetary Science Institute meeting paper (Piersol and Sprenke, 2014) and is written in a form for future publication in the journal *Icarus*.

For my best friend and wife,

Ann Godoy Piersol.

Without her this journey would

have been impossible,

and more importantly, unbearable.

Table of Contents

List of Tables

List of Figures

Chapter 1: On a common mantle source for Snake River Plain and Saddle Mountain basalts

ABSTRACT

The western Snake River plain (WSRP) of Idaho and Oregon erupted relatively homogenous olivine tholeiites in a period starting somewhat before 11 Ma and continuing to 7 Ma with an upsurge in the period from 9-7 Ma. Starting at 2.2 Ma a spike in WSRP volcanism again produced homogenous olivine tholeiites until 0.9 Ma which appear to be derived from the same subcontinental lithospheric mantle source (White et al, 2002). In addition, the Saddle Mountain Asotin Member basalts erupted at 13 Ma, three of the Weissenfels Ridge member basalts erupted between 13 and 12 Ma, the Ice Harbor Member basalts erupted at 8.8-8.5 Ma, and central and eastern Snake River plain (ESRP) basalts ranging in age from 12.8 Ma to Holocene, are also found to be derived from the same mantle source as these WSRP basalts.

A model is proposed invoking focused non-thermal mantle upwellings generated by the leading and northwest edges of the subducting Farallon plate fragment imaged by James et al. (2011) that induce partial melting of the subcontinental lithosphere northwest in the WSRP resulting in the 9-7 Ma period of upsurge in basaltic volcanism (Faccenna et al., 2010). As suggested by James et al. (2011) these edge generated upwellings continued to induce partial melting in the ESRP from the mid-Miocene to the Holocene. Similar focused non-thermal mantle upwellings are invoked that result in the partial melting of the common mantle source and the eruption of the Saddle Mountain basalts. These upwellings were generated by surviving plate fragments following the destruction of the Juan de Fuca plate at 17 Ma when the trapped Yellowstone plume head broke through the subducting plate (Geist and Richards, 1993; Xue and Allen, 2007).

INTRODUCTION

Neogene magmatism in the U.S. Pacific Northwest is one of the most vigorous igneous events to have occurred anywhere on the continents. The province includes the Columbia River Basalt Group (CRBG) of Washington, Oregon, and western Idaho and the nearby eastern Snake River Plain (ESRP) in southeast Idaho (Hooper, 1997). The CRBG erupted an estimated total of 210,000 km^3 from 16.8 to 6.2 Ma onto the Columbia Plateau, making it a relatively small example of a large igneous province. The last phase of the CRBG, the Saddle Mountain Basalt (SMB), erupted between 14.57 and 6.2 Ma and constitutes less than 1.1% of the CRBG volume. The Saddle Mountain Basalts are not simply related to the more voluminous earlier CRBG basalts (Barry et al., 2013; Hooper, 1997; Hooper and Hawkesworth, 1993; Jarboe et al., 2008; Jarboe et al., 2010; Reidel et al., 2013, Swanson et al., 1979, Tolan et al., 1989) as the geochemical source component of the SMB does not appear in the earlier CRBG basalts (Carlson, 1984). Many hypotheses have been proposed to explain the origin of the CRBG. Some attribute the CRBG to back-arc extension, perhaps linked to slab roll-back in the Cascades Arc, or upper mantle convection (Carlson, 1984; Christiansen et al., 2002; Humphreys et al., 2000; King and Anderson, 1995). Others attribute the CRBG to a plume originating in the deep mantle (Morgan, 1972; Pierce and Morgan, 1992, 2009; Wolff et al., 2008).

The western Snake River Plain (WSRP) is a fault bounded graben, located between the Columbia Plateau and the ESRP (Wood and Clemens, 2002). It is oriented orthogonal to the ESRP, trending northwest towards the Columbia Plateau. Its genesis is uncertain though some have argued that it is related to the plume responsible for the CRBG (Geist and Richards, 1993; Shervais and Hanan, 2008); others associate its origin to Basin and Range extension (Hooper et al., 2002; Shervais et al., 2002).

The plume hypothesis links the CRBG to the ESRP via a proposed hotspot track through the ESRP to the present day Yellowstone caldera (Armstrong et al., 1975; Morgan, 1972). According to the plume hypothesis the early most voluminous flows of the CRBG (Steens, Imnaha, and Grande

Ronde) are the result of the eruption of plume material that was deflected north, perhaps underneath the subducting Farallon plate or by following a northward trending rift system (Geist and Richards, 1993; Pierce and Morgan, 1992; Takahashi et al., 1998). The eruption of the CRBG by lateral transport through an extensive dike system from a central magma chamber may also be involved (Wolff et al., 2008).

This paper focuses on the younger episodes of magmatism in the CRBG and Snake River Plain (SRP). Many basalts of the Saddle Mountain group and Snake River Plain (SRP) are compositionally similar and penecontemporaneous (Carlson, 1984; Shervais, 2002). This work uses published data to compare the compositions of the Saddle Mountain basalts (Helz, 1978; Hooper, 2000), basalts of the WSRP (Clemens, 1993; White et al., 2002), and basalts of the central and ESRP (Honjo, 1986; Hughes et al., 2002; Kauffman, 2007; Knobel et al., 1995; Kuntz et al., 1992; Leeman and Vitaliano, 1976; Lum et al., 1989; USGS) and presents a melting model that is used to demonstrate a common mantle source. $^{87}Sr/^{86}Sr$ data for the Saddle Mountain basalts are compiled from Carlson et al. (1981), Carlson (1984), Helz (1978), Hooper and Hawkesworth (1993), McDougall (1976), and Nelson (1980).

Snake River Plain

The WSRP of southwest Idaho and eastern Oregon is approximately 70 km wide and 300 km long with the long axis trending approximately N40°W (Figure 1.1). It is a fault bounded graben with slip ranging from approximately 2-4 km along the steeply dipping faults (Wood and Clemens, 2002). Most faulting began at approximately 11 Ma and essentially ended by 9 Ma, which corresponds to the initiation of extensive basaltic volcanism throughout the WSRP from 9-7 Ma. The axis of the WSRP is characterized by positive gravity (approximately 100 milligals) and magnetic anomalies that have been interpreted as dense (2.9 g/cm^3) mafic intrusions into the crust at 9-18 km and 3-6 km (Mabey, 1976, 1982; Wood and Clemens, 2002). Wood and Clemens (2002) estimated extension of the WSRP

to be between 3 and 10 percent. The WSRP cuts the Cretaceous Atlanta lobe of the Idaho Batholith and is also bounded by 12 to 10 Ma rhyolites.

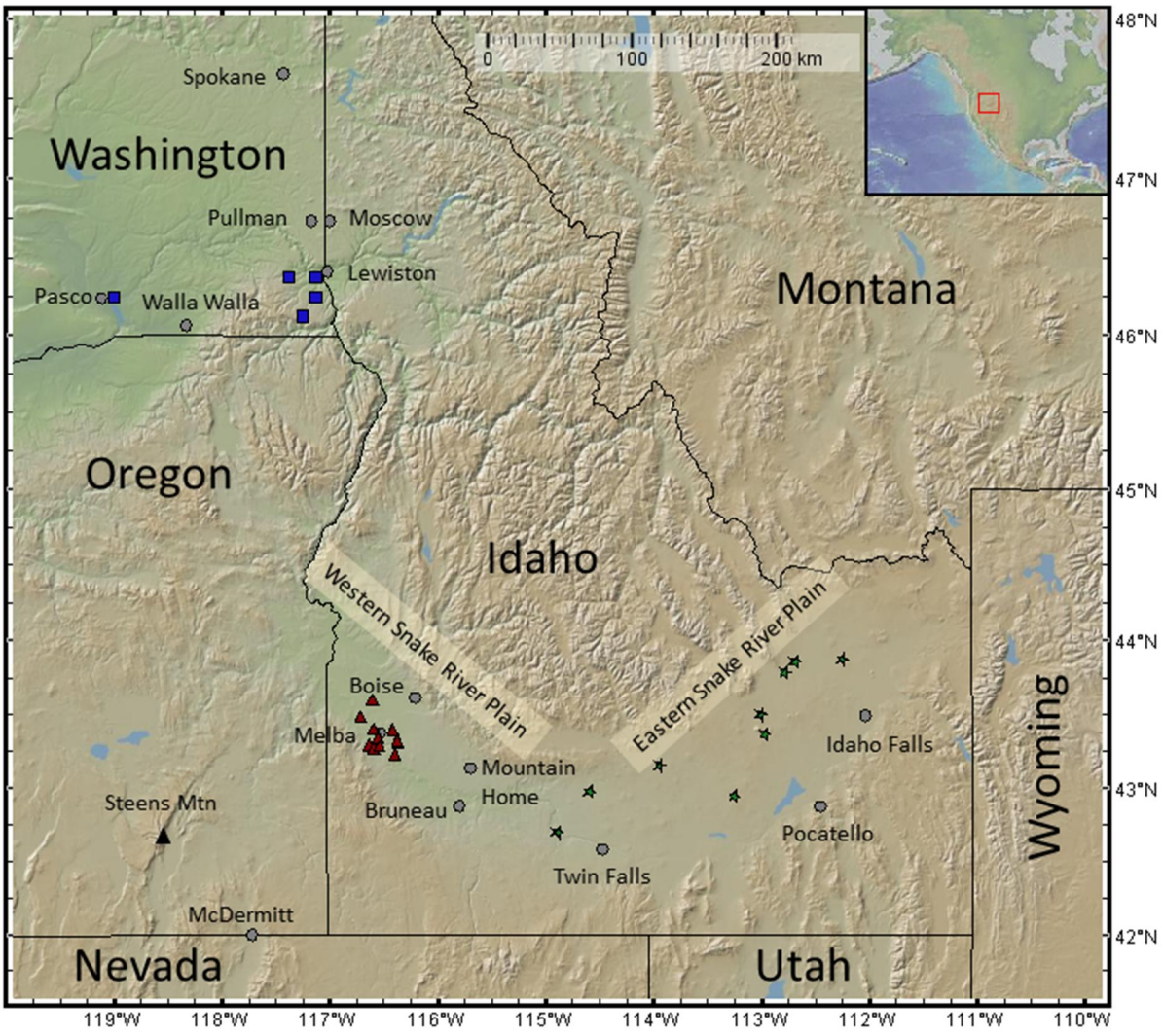

Figure 1.1. Locations of compositionally similar basalts with measured $^{87}Sr/^{86}Sr$ referenced in the text. The WSRP M1 and M2 basalts are located near the town of Melba southwest of Boise and depicted by red triangles. Green stars depict the location of central and ESRP basalts shown in Figure 1.8. The locations of Saddle Mountain basalts are depicted by blue squares with the Ice Harbor Member basalts near Pasco and the Weissenfels and Asotin Member basalts southwest of Lewiston. Figure generated with GeoMapApp, http://www.geomapapp.org (Ryan et al., 2009).

Clemens (1993) describes 13.5 ± 2.5 Ma basalts, retrieved from the J.N. James Well near Meridian Idaho at 13380-13480 ft. depth that are compositionally similar to the basalts erupted in the

9 to 7 Ma period. After 7 Ma volcanism appears to have been relatively quiescent until its resumption at about 2.2 Ma. This second active period produced basalt until about 0.4 Ma. White et al. (2002) analyzed basalts from the entire WSRP eruptive history in a 1000 square kilometer area around the town of Melba, ID in the south-central WSRP. They categorized them into 3 groups, M1, M2, and M3, on the basis of age and alkalinity. The M1 olivine tholeiites erupted in the 9-7 Ma period. Starting at approximately 2.2 Ma until 0.9 Ma the M2 olivine tholeiites erupted. White et al. (2002) demonstrated through mass-balance and MELTS modeling that the M2 basalts can be related to the M1 basalts through a common mantle source by fractional crystallization of approximately 35% plagioclase (An_{61}), 13% olivine (Fo_{71}), and 8% augite (En_{35}), at about 0.3 GPa, consistent with the depth of the gravity high (Mabey, 1976, 1982). From approximately 0.8 to 0.4 Ma the M3 basalts erupted; these basalts are more alkaline than the M1/M2 basalts and are attributed to a deeper mantle source (Shervais and Vetter, 2009; White et al., 2002).

Shervais et al. (2002) noted that the WSRP is aligned radially with respect to the Columbia Plateau of Washington and Oregon and suggested that the WSRP rifting was initiated by thermal doming of the Columbia Plateau by a deflected plume (Geist and Richards, 1993) accompanied later by thermal softening of the lithosphere (12.5-11 Ma) centered at the Bruneau-Jarbidge eruptive center to the south of the WSRP. Alternatively, Hooper et al. (2002) described right-lateral displacement at the northwest end of the WSRP in the region of the Oregon-Idaho Graben and argued that the formation of the WSRP is related to Basin and Range extension. Wolff et al. (2008) suggested a region in eastern Oregon at the confluence of the northwest end of the WSRP, the northern end of the Oregon-Idaho graben, and southern extent of CRBG dike swarms to be the location of a giant magma chamber that was the source of the main phase of the CRBG, tectonically relating the WSRP to CRBG volcanism.

Unlike the fault-bounded rift graben of the WSRP, the eastern Snake River Plain (ESRP) is downwarped, perhaps due to loading by a mid-crustal mafic sill and thermal subsidence away from

the Yellowstone hotspot (McQuarrie and Rodgers, 1998; Rodgers et al., 2002; Shervais et al., 2006). The formation of the ESRP has been ascribed to the passage of the North American plate over a mantle plume that is currently located under the Yellowstone caldera in Wyoming (Armstrong et al., 1975; Braile et al., 1982; Morgan, 1972; Pierce and Morgan, 1992, 2009). The main evidence for this hypothesis is the time progressive-sequence of rhyolite volcanism starting at approximately 16.1 Ma in the McDermitt volcanic field straddling the Oregon/Nevada border, progressing to the northeast through the ESRP and ending at the present day Yellowstone caldera (Figure 1.1). More recently Coble and Mahood (2012) locate the impingement of the plume to be centered on Steens Mountain with volcanism initiating there at approximately 16.7 Ma (Figure 1.1). Others propose that the initial plume head may have been trapped beneath the subducting Farallon plate and deflected north before breaking through the plate at approximately 17 Ma, erupting the most voluminous members of the Columbia River Basalt Group (CRBG) (Geist and Richards, 1993; Xue and Allen, 2007).

James et al. (2011) have published seismic tomographic images of what they interpret is a slab fragment underneath and aligned with the ESRP (Figure 1.2). The slab is situated with the northwest edge of the slab imaged at or slightly above 400 km directly under the ESRP and then extending down towards the southeast to approximately 700 km depth. A sheet of low velocity mantle extends from the transition zone upwards around the northern edge of the slab, and into a ~-2% S-wave low velocity zone that extends along the entire 400-500 km length of the ESRP at a depth of approximately 150-200 km. They interpret this sheet of low velocity mantle as a curtain of mantle upwelling generated by the slab fragment (Faccenna et al., 2010). The numerical models of Faccenna et al. (2010) suggest that sheet-like upwellings can be generated on the order of 100 km away from the edges of a slab or slab fragment. James et al. (2011) suggest that the presence of this sheet-like mantle upwelling is responsible for the continued basaltic volcanism in the ESRP long after the passage of the proposed Yellowstone hotspot track.

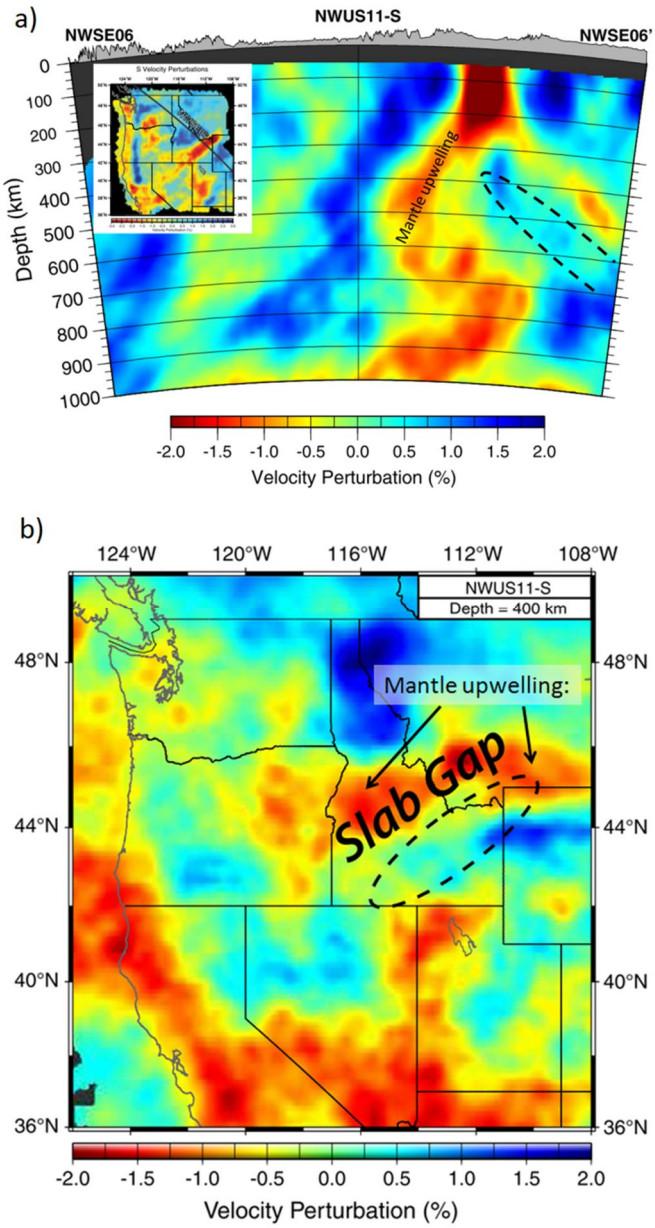

Figure 1.2 (Modified from James et al, 2011). S-wave tomographic imaged slab fragment beneath the ESRP. a) A transect across the central ESRP from northwest on the left to southeast on the right. The red zone is interpreted as a sheet of low velocity focused mantle upwelling curving upwards and around the northwest edge of a slab fragment depicted approximately by dashed black line. The dark red zone is a strong S-wave low velocity zone beneath the ESRP. b) Dashed black line approximately outlines slab fragment at 400 km depth. Sheet of mantle upwelling seen northwest of slab in slab gap.

Saddle Mountain Basalts

The Columbia River Basalt Group (CRBG) is a large igneous province located in Washington, Oregon, and Idaho (Figure 1.3). It comprises seven formations the earliest six of which, the Steens Basalt, Imnaha Basalt, Grande Ronde Basalt, Picture Gorge Basalt, Prineville Basalt, and the Wanapum Basalt erupted from 16.8 to 15 Ma and represent approximately 98.9% of the volume of the CRBG. The seventh formation is the Saddle Mountain Basalt (SMB), which erupted from 14.57 to 6.2 Ma (Barry et al., 2013, Carlson, 1984; Hooper, 1997; Hooper and Hawkesworth, 1993; Reidel et al., 2013; Swanson et al., 1979; Tolan et al., 1989). The wide range in isotopic and geochemical compositions of the SMB imply that they are derived from a different mantle source or sources than are the earlier more voluminous CRBG basalts (Carlson, 1984; Carlson et al., 1981; Church, 1976). Carlson (1984) and Hooper and Hawkesworth (1993) conclude that the $^{87}Sr/^{86}Sr$ variations in the SMB can be ascribed to a subcontinental lithospheric mantle source enriched in incompatible trace elements at approximately 2-2.6 Ga.

The SMB represent less than 1.1% of the total estimated 210,000 km^3 volume of the CRBG and most fill low-lying terrain such as the ancestral Snake River Canyon rather than as extensive sheet flows such as those characterizing the earlier Grande Ronde and Wanapum basalts (Reidel et al., 2013; Swanson et al., 1979). Some of the oldest SMB members, Umatilla, Wilbur Creek, and Asotin, are found conformable with the earlier Wanapum Basalt, however (Barry et al., 2013; Reidel et al., 2013; Swanson et al., 1979; Tolan et al., 1989). Vents for the SMB are located in the northern half of the Chief Joseph Dike Swarm and most flows can be traced back to a region near the confluence of the Washington, Oregon, and Idaho borders or to the Lewiston Basin slightly to the north (Figure 1.1). Exceptions include the Ice Harbor Member basalts at 8.8-8.5 Ma, with vents in the environs of the Tri-Cities area of Washington, and the Esquatzel Member basalts (13-10.65 Ma) whose vents are thought to be located in the eastern Columbia Plateau. The vents of the Pomona Member flows (12-10.85 Ma) are located in western Idaho (Reidel et al., 2013; Swanson et al., 1979).

Columbia River Basalt Group			
Formation		Member	Isotopic Age, Ma
Saddle Mountains Basalt		Lower Monumental Member	6.2
		Ice Harbor Member	8.8 - 8.5
		Basalt of Goose Island	
		Basalt of Martindale	
		Basalt of Basin City	
		Buford Member	
		Elephant Mountain Member	10.5 - 10
		Weippe Member	
		Pomona Member	12 - 10.85
		Esquatzel Member	13 - 10.65
		Weissenfels Ridge Member	
		Basalt of Slippery Creek	
		Basalt of Tenmile Creek	
		Basalt of Lewiston Orchards	
		Basalt of Cloverland	
		Asotin Member	
		Basalt of Huntzinger	
		Basalt of Lapwai	
		Wilbur Creek Member	13.3
		Basalt of Wahluke	
		Umatilla Member	14.57
		Basalt of Sillusi	
		Basalt of Umatilla	
Wanapum Basalt		...	15.6 - 15.0
Prineville Basalt	Grande Ronde Basalt	...	16.0 - 15.6
Picture Gorge Basalt			
Imnaha Basalt		...	16.7 - 16.0
Steens Basalt		...	16.8 - 16.6

Figure 1.3. Ages of Saddle Mountain Basalts in relation to the Columbia River Basalt Group (Barry et al., 2013, Reidel et al., 2013).

GEOCHEMISTRY OF SRP AND SADDLE MOUNTAIN BASALTS

Strontium Isotope Ratios

$^{87}Sr/^{86}Sr$ of Saddle Mountain basalts range widely (Figure 1.4). This variation is not correlated with age or composition (Figure 1.5) (Hooper, 1984; Hooper and Swanson, 1990). Major element composition is also not correlated with $^{87}Sr/^{86}Sr$, as the Asotin Member, one of the least evolved lavas, and basalt of Goose Island, one of the most evolved lavas, have similar $^{87}Sr/^{86}Sr$. Lower Monumental Member lavas, with Mg concentrations intermediate between Asotin and Goose Island, have the highest $^{87}Sr/^{86}Sr$ of all Saddle Mountain basalts. The WSRP M1 and M2 basalts, along with the Saddle Mountain Ice Harbor Member, Buford Member, Elephant Mountain Member, Pomona Member, Weissenfels Ridge Member (with the exception of the basalt of Slippery Creek), and the Asotin Member basalts have similar $^{87}Sr/^{86}Sr$, all below approximately 0.708.

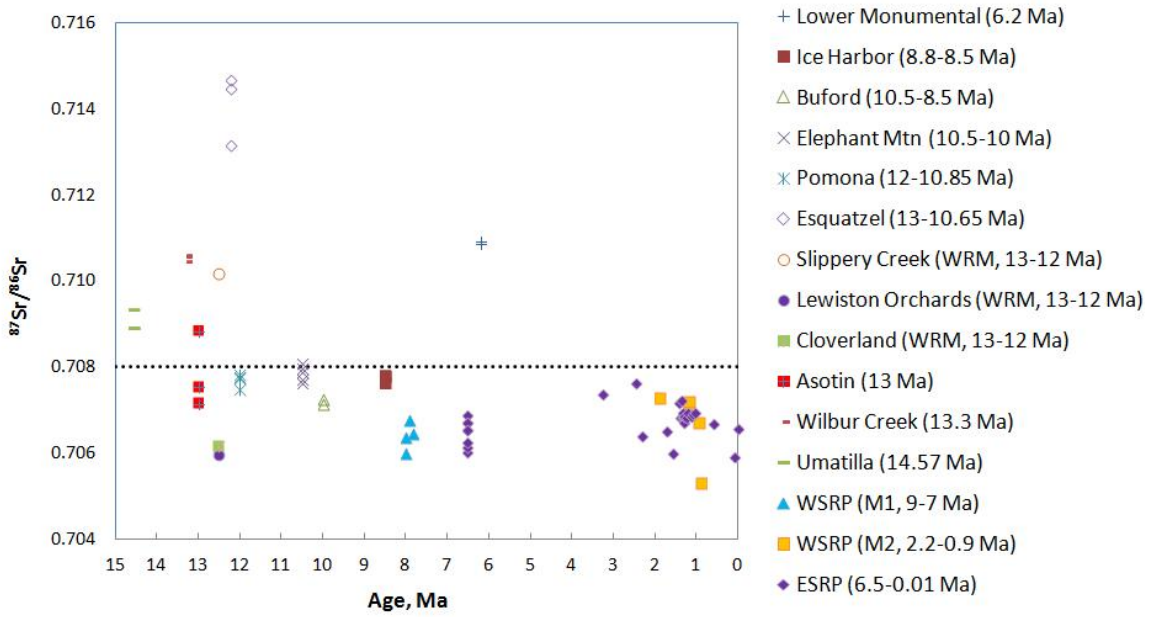

Figure 1.4. $^{87}Sr/^{86}Sr$ versus age of Saddle Mountain and SRP basalts. Ice Harbor includes Goose Island, Martindale, and Basin City basalts. WRM indicates Weissenfels Ridge Member.

Major and Trace Elements

Major element compositions of SRP and SMB broadly overlap and range from the most primitive Asotin Member basalts to the most evolved Umatilla Member basalts. With decreasing Mg#, the Saddle Mountain basalts and the SRP basalts exhibit similar increasing trends in Na, K, and P. Exceptions are slightly high Na for the Umatilla Member basalts, slightly high K for the Umatilla, Wilber Creek, and Buford Member basalts, and slightly low P for the Umatilla, Elephant Mountain, Esquatzel, and Buford Member basalts. All basalts exhibit a similar correlation between Ca and Mg#, and, with the exception of the Umatilla Member basalts, Al also correlates to Mg#. Increasing concentrations of Ti, Fe, and Mn with decreasing Mg# are similar in all basalts with the exception of the more variable Umatilla Member lavas. All basalts display a decreasing trend of CaO/Al_2O_3 with decreasing Mg#, and ratios of Sc/Y versus Sr/Y correlate. Ba/Nb is not correlated to La/Y (an indicator of melting in the presence of garnet) for the SRP and most Saddle Mountain basalts, but Ba/Nb of most Saddle Mountain basalts is similar to that of the SRP basalts. Exceptions include higher Ba/Nb of the Wilbur Creek Member, some of the Asotin Member basalts, and basalt of Eden, and very high Ba/Nb of the Umatilla Member basalts. The Elephant Mountain Member and the basalt of Cloverland have variable Ba/Nb. The WSRP M2 basalts and basalt of Martindale have similar major element compositions.

When normalized to primitive mantle all of the Saddle Mountain basalts and sampled SRP basalts have negative Sr anomalies (Figure 1.6) (Sun and McDonough, 1989). All of the basalts have anomalously high Pb, and most have positive Ba anomalies.

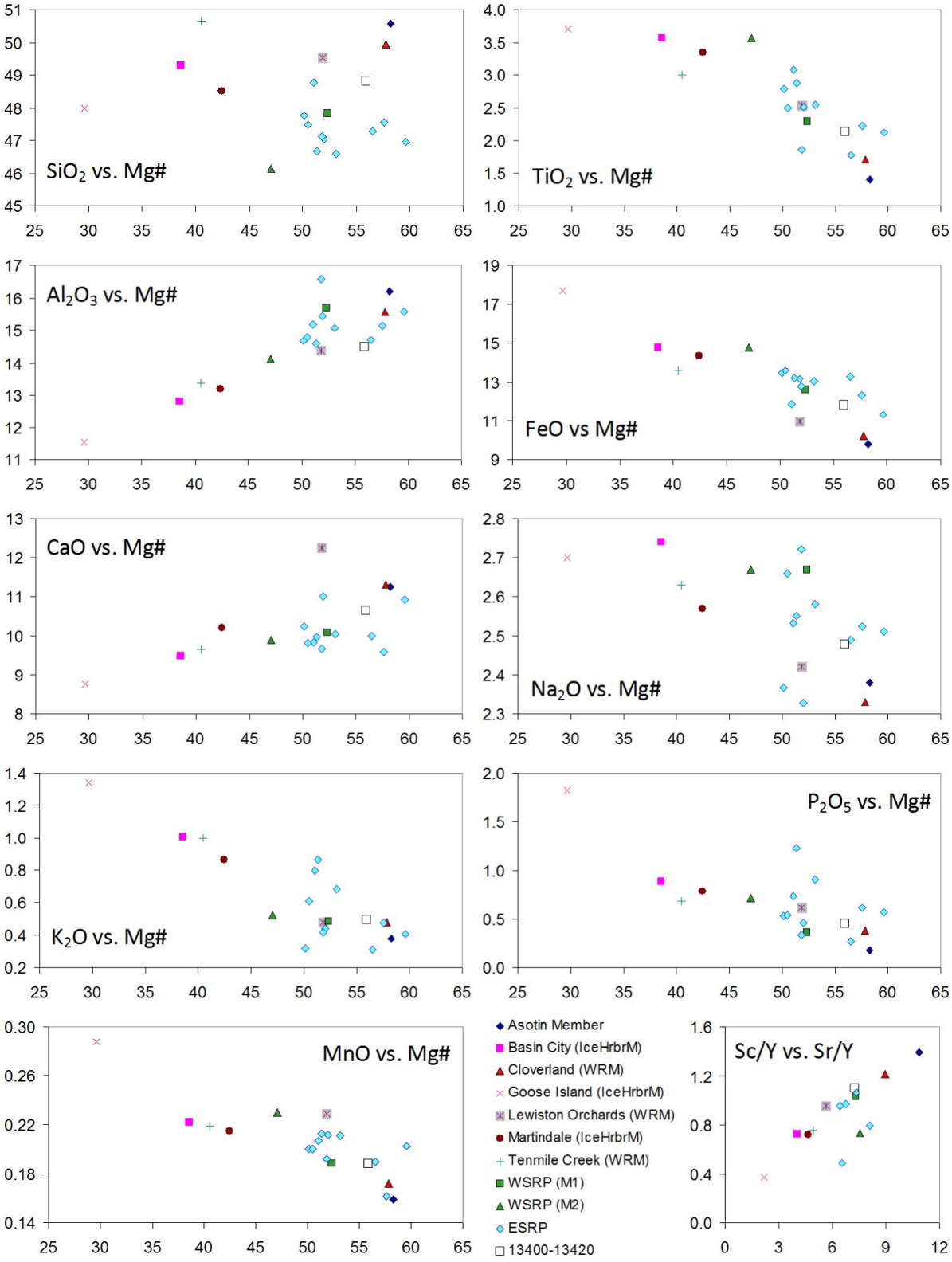

Figure 1.5. Composition of low $^{87}Sr/^{86}Sr$ Saddle Mountain and SRP basalts. The same samples are depicted in figures 1.6, 1.7, and 1.8.

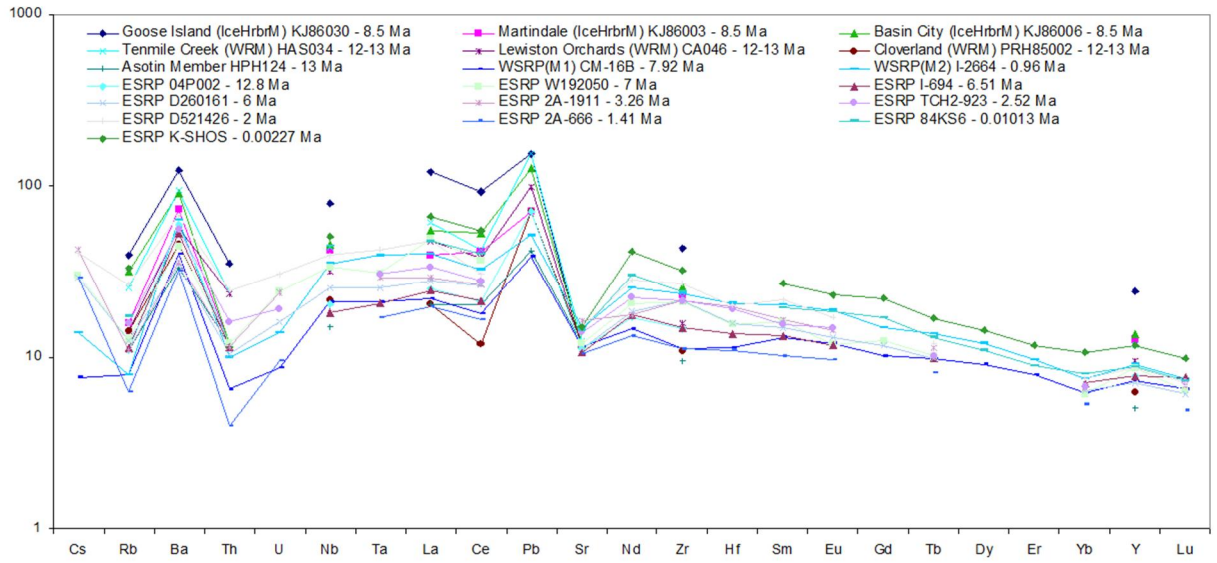

Figure 1.6. Primitive mantle (Sun and McDonough, 1989) normalized trace elements of selected Saddle Mountain and SRP basalts.

	Cs	Rb	Ba	Th	U	Nb	La	Ce
Olivine	0.05 [26]	0.00018 [20]	0.000032 [4]	0.0000293 [3]	0.00001 [3]	0.01 [20]	0.0001 [23]	0.0001 [23]
Orthopyroxene	0.0009 [1]	0.0006 [20]	0.0036 [1]	0.0002 [24]	0.0001 [20]	0.0013 [12]	0.0008 [12]	0.0016 [12]
Clinopyroxene	0.0058 [15]	0.011 [20]	0.00068 [14]	0.00041 [3]	0.00006 [15]	0.06 [16]	0.0536 [14]	0.0858 [14]
Plagioclase	0.1091 [5]	0.093 [2]	0.504 [5]	0.173 [2]	0.105 [2]	0.029 [2]	0.27 [6]	0.233 [5]
	Pb	**Pr**	**Sr**	**Nd**	**Zr**	**Hf**	**Sm**	**Eu**
Olivine	0.000069 [3]	0.0002 [23]	0.00025 [4]	0.0003 [23]	0.025 [11]	0.01 [20]	0.0011 [23]	0.001 [23]
Orthopyroxene	0.0013 [20]	0.0032 [12]	0.0012 [12]	0.0056 [12]	0.032 [12]	0.06 [12]	0.015 [12]	0.03 [12]
Clinopyroxene	0.0102 [15]	0.112 [25]	0.052 [25]	0.201 [25]	0.123 [14]	0.24 [16]	0.291 [14]	0.32 [17]
Plagioclase	0.431 [5]	0.142 [5]	1.715 [2]	0.124 [5]	0.0127 [5]	0.026 [2]	0.106 [5]	0.616 [5]
	Gd	**Tb**	**Dy**	**Ho**	**Er**	**Yb**	**Y**	**Lu**
Olivine	0.0029 [23]	0.0015 [23]	0.002 [23]	0.0047 [4]	0.0025 [23]	0.01 [23]	0.0036 [23]	0.045 [8]
Orthopyroxene	0.034 [12]	0.054 [12]	0.077 [12]	0.1 [12]	0.12 [12]	0.22 [12]	0.095 [12]	0.22 [12]
Clinopyroxene	0.24 [13]	0.28 [25]	0.38 [17]	0.25 [12]	0.37 [17]	0.38 [13]	0.467 [14]	0.433 [14]
Plagioclase	0.0502 [6]	0.029 [2]	0.0318 [6]	0.02 [2]	0.024 [2]	0.03 [2]	0.031 [5]	0.024 [2]
	Tm	**Sc**	**V**	**Cr**	**Ni**	**Cu**	**Zn**	
Olivine	0.003 [23]	0.29 [23]	0.09 [9]	1.18 [18]	12.8 [22]	0.55 [18]	0.8 [19]	
Orthopyroxene	0.071 [12]	0.64 [1]	1.65 [1]	7.78 [1]	11.3 [1]	2.8 [1]	0.66 [1]	
Clinopyroxene	0.255 [25]	1.31 [14]	3.1 [14]	3.8 [14]	2.6 [21]	0.36 [14]	0.5 [7]	
Plagioclase	0.049 [2]	1.458 [5]	0.27 [5]	0.191 [5]	1.16 [5]	0.17 [7]	0.11 [7]	

Table 1.1. Partition coefficients used in the melt model (Geochemical Earth Reference Model database http://earthref.org/GERM/). Sources are listed in parentheses as follows: (1) Adam & Green, 2006; (2) Aignertorres et al., 2007; (3) Beattie, 1993; (4) Beattie, 1994; (5) Bindeman et al., 1998; (6) Bindeman & Davis, 2000; (7) Bougault & Hekinian, 1974; (8) Dunn, 1987; (9) Duke, 1976; (10) Forsythe et al., 1994; (11) Fujimaki et al., 1984; (12) Green et al., 2000; (13) Hack et al., 1994; (14) Hart & Dunn, 1993; (15) Hauri et al., 1994; (16) Johnson & Kinzler, 1989; (17) Johnson, 1998; (18) Kloeck & Palme, 1988; (19) Kloeck & Palme, 1989; (20) McKenzie & O'Nions, 1991; (21) Mysen, 1978; (22) Nabelek, 1980; (23) Nielsen et al., 1992; (24) Salters & Longhi, 1999; (25) Shulski et al., 1994; (26) Villemant et al., 1981.

MELT MODEL

Introduction

The observation that many SRP and SMB have similar $^{87}Sr/^{86}Sr$ suggests that they may be derived from a common mantle source (there are no published Pb or Nd isotopic data on these WSRP samples). Our approach is to assess SRP Saddle Mountain basalts with $^{87}Sr/^{86}Sr < 0.708$ to determine whether they may have been produced by different extents of partial melting of a common, or very similar, mantle source. The model first corrects for crystallization then tests the hypothesis that the magmas are related by variable extents of partial melting of the same, or very similar, mantle source followed by crystallization.

Calculations

Batch partial melting of the mantle partitions trace elements into the liquid according to the equation (Shaw, 1970):

$$\frac{C_{lm}}{C_{om}} = \frac{1}{D_m(1 - F_m) + F_m} \quad (1)$$

In equation 1, C_{lm} is the trace element concentration in the melt, C_{om} is the original trace element concentration in the solid, D_m is the bulk distribution coefficient, and F_m is the melt fraction. The subscript m is used to represent mantle source and to differentiate the components in equation (1) from those used in the Rayleigh Fractionation equation (4) below that use the subscript f.

In this study the WSRP sample 13400-13420 is used to calculate a hypothetical mantle source (Clemens, 1993). This sample is an olivine tholeiite retrieved from a well drilled in the WSRP west of Boise near Meridian Idaho at 13400-13420 feet depth. It was chosen as the basis for comparison because it is the oldest sample investigated. Making the arbitrary assumption that the sample 13400-13420 represents a 10% partial melt of a mantle source, and that little to no subsequent crustal

contamination took place, one can calculate a hypothetical source mantle trace element composition by manipulating equation 1 to this form:

$$C_{om} = C_{lm}(D_m(1 - F_m) + F_m) \quad (2)$$

Likewise, one can determine the amount of partial melting of the hypothetical mantle source by manipulating equation 1 to this form calculating from any trace element; this study used Nb or Ta:

$$F_m = \left(\frac{C_{om}}{C_{lm}} - D_m\right)\left(\frac{1}{1 - D_m}\right) \quad (3)$$

To model for the effect of Rayleigh fractionation on trace element concentrations in a partial mantle melt the following equation is used:

$$\frac{C_{lf}}{C_{of}} = F_f^{D_f - 1} \quad (4)$$

In equation 4, C_{lf} is the trace element concentration in the melt after fractionation of solids, C_{of} is the original trace element concentration in the melt before fractionation, D_f is the bulk distribution coefficient, and F_f is the fraction of the melt remaining.

If one assumes that an original partial mantle melt rises into the lithosphere and subsequently undergoes Rayleigh fractionation with little to no crustal contamination, one can relate equation 1 to equation 4 by the fact that C_{lm} must equal C_{of}. From equation 4 we find:

$$C_{of} = \frac{C_{lf}}{F_f^{D_f - 1}} \quad (5)$$

One can determine the amount of partial melting by substituting the right side of equation 5 for C_{lm} in equation 3:

$$F_m = \left(\frac{C_{om}}{\frac{C_{lf}}{F_f^{D_f - 1}}} - D_m\right)\left(\frac{1}{1 - D_m}\right) \quad (6)$$

Implementation with a WSRP basalt sample

A hypothetical mantle source was calculated using equation (2) with an arbitrary F_m of 0.1 for WSRP sample 13400-13420 and the assumption that little to no crustal contamination had affected the sample. The mode of the source is assumed to be 60% olivine, 30% orthopyroxene, and 10% clinopyroxene to calculate the bulk distribution melting coefficient D_m using partition coefficients obtained from the Geochemical Earth Reference Model database (GERM) (Table 1.1). When available, partition coefficients based on experimental results were selected. Occasionally, more than one result was available so, to maintain model consistency, the partition coefficient closest to the results of McKenzie and O'Nions (1991) was selected.

Equation (6) was used to calculate melt fraction of each SRP and Saddle Mountain sample used in this study using the same bulk distribution melting coefficient D_m. The extent of fractional crystallization F_f was determined by calibrating Mg# using the MELTS program of Ghiorso and Sack (1995). The model is calculated at 0.3 GPa as suggested by White et al. (2002). The Mg# of the evolved rocks were then compared to the Mg# of the liquids of the MELTS output to estimate F_f of the rocks. D_f was estimated using the MELTS output proportions of fractionating solids of approximately 15% olivine, 35% clinopyroxene, and 50% plagioclase. As noted by White et al. (2002), none of these WSRP basalts contain pyroxene phenocrysts. White et al. (2002) suggest that this occurs because at 0.3 GPa approximately 80% of the clinopyroxene fractionates within a temperature range of only two degrees; the rapid removal of this clinopyroxene and subsequent rise of magmas into shallow subvolcanic chambers would account for the lack of pyroxene phenocrysts. Because all of the elements are incompatible, small differences in the mode are of little consequence to the model. Then, using Nb concentrations for C_{lf}, F_m was calculated for each sample; where Nb concentrations are unavailable Ta was used instead. The C_{lm} of all other incompatible trace elements for each sample was calculated using this modification of equation (1):

$$C_{lm} = \frac{C_{om}}{D_m(1 - F_m) + F_m} \tag{7}$$

Using the F_f determined from MELTS output the C_{lf} for each available trace element in each sample was calculated from this modification of equation (4):

$$C_{lf} = C_{of}\left(F_f^{D_f-1}\right) \quad (8)$$

In order to estimate the ideal extents of partial melting, the residuals between the calculated C_{lf} and the actual sample trace element concentration were normalized to the calculated C_{lf} and then squared and summed to estimate the composition of hypothetical melts that most closely match the natural rocks. The sample with the lowest sum of the square of normalized residuals for each formation member is plotted (Figures 1.7 and 1.8) in a normalized incompatible element diagram (normalized to the primitive mantle of Sun and McDonough, 1989) along with the calculated trace element concentrations. These best-fit samples are the same as those plotted in Figures 1.5 and 1.6. Because it was used to calculate the extent of melting, Nb or Ta matches perfectly.

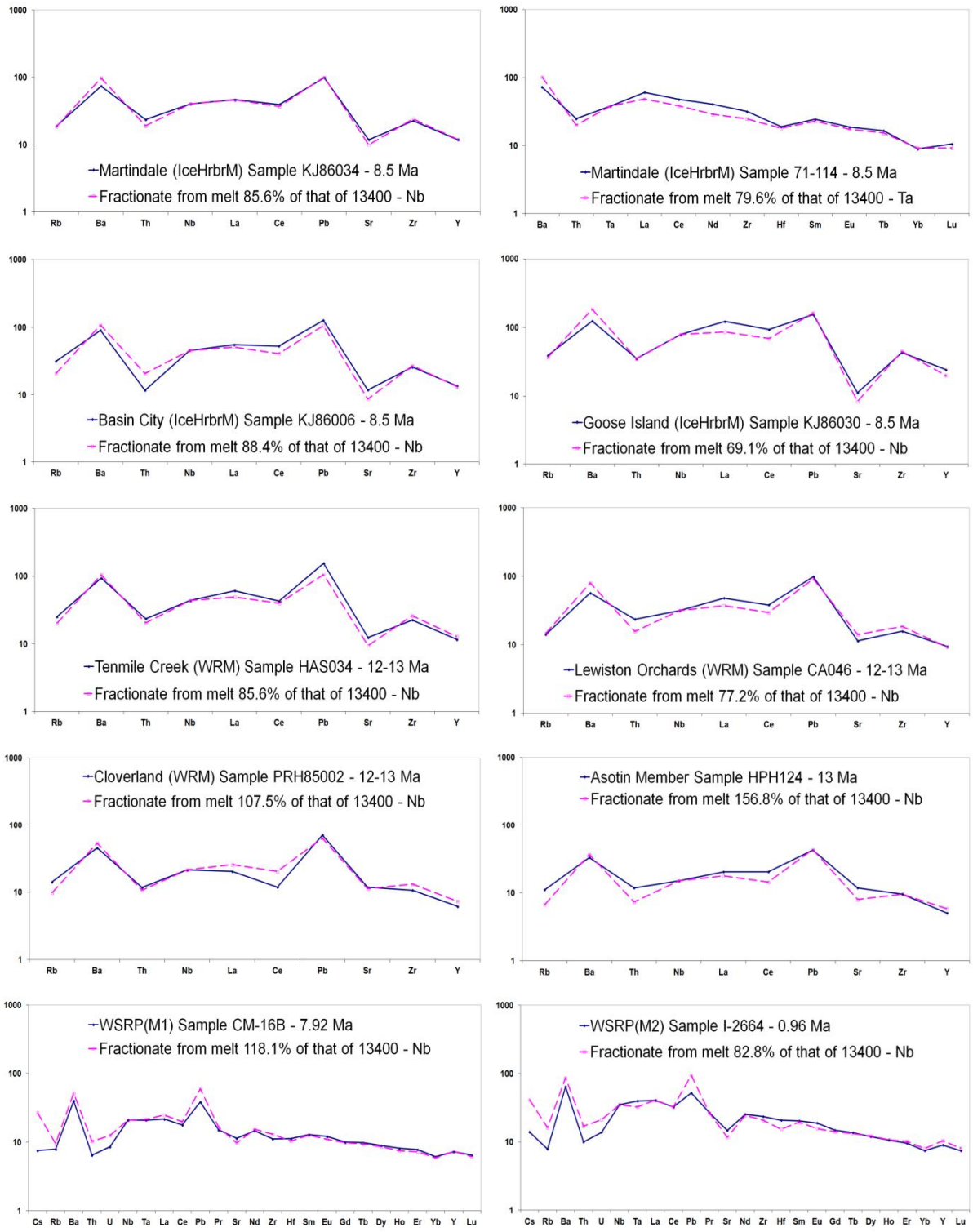

Figure 1.7. Saddle Mountain and WSRP best-fit trace element diagrams with calculated trace elements from melt model normalized to primitive mantle (Sun and McDonough, 1989). The melt model calculated trace elements are plotted with red dashed lines with best-fit sample trace element data depicted in solid black.

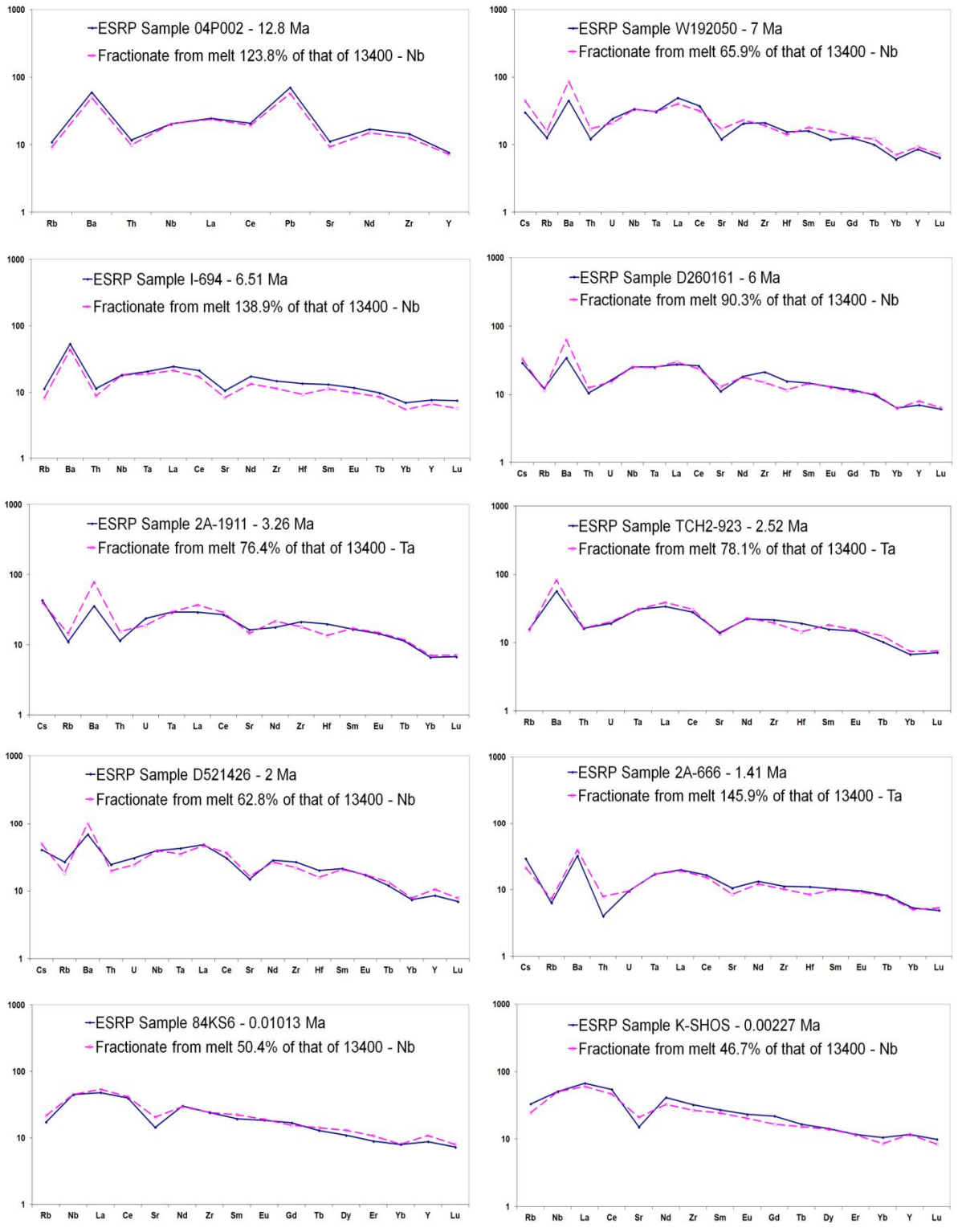

Figure 1.8. Central and ESRP best-fit trace element diagrams with calculated trace elements from melt model normalized to primitive mantle (Sun and McDonough, 1989). The symbology is the same as is used in Figure 1.7.

DISCUSSION

The compositions of the three Ice Harbor Member basalts (SMB), Martindale, Basin City, and Goose Island, correspond closely to the calculated trace element concentrations derived from the hypothetical mantle source for WSRP sample 13400-13420 (Figure 1.7). Likewise, three Weissenfels Ridge Member basalts of the SMB (Tenmile Creek, Lewiston Orchards, and Cloverland), the Asotin Member basalts, the two WSRP basalt groups M1 and M2, and many central and ESRP mid-Miocene to Holocene basalts all closely correlate to the trace element melt model (Figure 1.8). This supports the hypothesis that these basalts are all derived from a common mantle source despite being erupted from vents hundreds of kilometers apart (Figure 1.1).

Of particular note are the Ice Harbor 8.8-8.5 Ma basalt of Basin City and the Weissenfels Ridge 13-12 Ma basalt of Tenmile Creek (both SMB). These two lavas are indistinguishable in both major and trace elements (Figure 1.5), and the melt model matches both basalts, with 13±1.4% lower extent of partial melting than sample 13400-13420. The vents for these two Saddle Mountain basalts are some 150 km apart and the eruptive events are separated by at least 3.2 Ma.

Three low $^{87}Sr/^{86}Sr$ Saddle Mountain basalts deviate significantly from the melt model calculated from trace elements. These are the Buford Member, the Elephant Mountain Member, and the Pomona Member. The deviation is strongest in the most incompatible trace elements. If these basalts are derived from the common mantle source then they have likely undergone crustal contamination. There is no notable difference in the major element compositions of these basalts, with the possible exception of P.

The 9-7 Ma period of basaltic volcanism in the WSRP produced rocks that have similar compositions, and this period of relatively homogenous compositions may extend from 11-7 Ma (White et al., 2002). From 2.2 to 1.0 Ma, another suite of WSRP basalts erupted, which has already been shown to be related to the older lavas from the same area (White et al., 2002). In fact, basalts

with similar composition are found throughout the WSRP. This implies a common mantle source for at least the central portion of the WSRP that has existed for at least the period of 11 to 1 Ma.

At approximately the same time that the oldest WSRP sample (13400-13420) erupted at 13.5 ± 2.5 Ma, the 13 Ma Asotin Member basalts (SMB) were erupting approximately 320 km to the north from vents in eastern Washington. Likewise, basalts erupted at 12.8 Ma in the central SRP (Kauffman, 2007), and between 13 and 12 Ma the Weissenfels Ridge Member basalts of Cloverland, Lewiston Orchards, and Tenmile Creek (all SMB) erupted. All of these basalts are derived from an indistinguishable mantle source despite being 100s of kilometers apart. Later, in the period from 9 to 7 Ma, the majority of the M1 basalts erupted, penecontemporaneously with the 8.8-8.5 Ma Ice Harbor Member basalts of Basin City, Martindale, and Goose Island, which erupted approximately 400 km north, and, as demonstrated here, from an indistinguishable mantle source. As basaltic volcanism waned in the WSRP, basalts that derive from the same indistinguishable mantle source erupted throughout the ESRP between 7 and 6 Ma (Lum et al., 1989; USGS). At approximately 3.5 Ma basalts derived from this mantle source again erupted in the central SRP (Kauffman, 2007) followed by eruptions throughout the ESRP with volcanism continuing into the Holocene (Hughes et al., 2002; Honjo, 1986; Kauffman, 2007; Knobel et al., 1995; Kuntz et al., 1992; Leeman and Vitaliano, 1976). Shortly thereafter, at 2.2 Ma, a 1.3 million year upsurge in basaltic volcanism erupted the M2 basalts in the WSRP, which, again, derive from the same long-lasting mantle source. Carlson (1984) defined a component of the CRBG as C3 with the Basalt of Martindale being representative of this component. He determined that this component was not present in the earlier basalts of the CRBG and that it most likely represented an enriched subcontinental lithospheric reservoir. We conclude that this component is the mantle source for the SMB and SRP basalts discussed in this study and that it must be geographically widespread throughout the Pacific Northwest.

The Miocene mantle source delineated in this study is not unlimited. It is distinguished from the mantle sources for the earlier CRBG and the high-alumina olivine tholeiites of the High Lava Plains

by higher $^{87}Sr/^{86}Sr$, REE concentrations, and light REE/heavy REE (Bailey and Conrey, 1992; Carlson, 1984; Hooper and Hawkesworth, 1993). Clearly, the main phase of the CRBG and High Lava Plains basalts derived from a different part of the mantle than the SMB.

One of the most important findings of this synthesis is that the edge of the North American craton, which transects the study area, does not appear to relate to the mantle source hypothesized here. The 0.706 $^{87}Sr/^{86}Sr$ isopleth for Mesozoic and Cenozoic siliceous rocks is clearly not a factor in the $^{87}Sr/^{86}Sr$ of SMB erupted to the west of the isopleth and SRP basalts erupted to the east of the isopleth. This suggests that the basalts derive from a sublithospheric source.

Recent tomographic images derived from data accumulated in the High Lava Plains seismic experiment and the EarthScope USArray Transportable Array indicate that much of the Pacific Northwest region, roughly centered on the High Lava Plains of Oregon and the Eastern Snake River Plain, appears to exhibit partial melting 5 to 10 kilometers below the Moho (Hanson-Hedgecock et al., 2012; Long et al., 2012; Till et al., 2013; Wagner et al., 2010; Wagner et al., 2012). This is interpreted to be partially melted mantle lithosphere, perhaps due to mantle upwelling (Faccenna et al., 2010).

Tectonic Models

Faccenna et al. (2010) concluded that focused mantle upwellings are generated up to ~100 km from the edges of a subducted slab. These focused upwellings are most vigorous upon initiation of subduction, when the leading edge of a slab reaches the mantle transition zone, and they are also created upon fragmentation of a subducting slab, which creates new edges that promote upwelling. Faccenna et al. (2010) proposed a regional model whereby the subducting Farallon slab reached the 660 km discontinuity in the vicinity of Steens Mountain at 17 Ma with the resulting increase in focused upwelling leading to decompression melting and the subsequent silicic volcanism along the

proposed hotspot track of Pierce and Morgan (1992) as well as the westward progression of the High Lava Plains of Oregon (Figure 1.1).

Similarly, James et al. (2011) proposed that the presumed Farallon plate slab fragment they have imaged under the ESRP (Figure 1.2) generates sheet-like mantle upwellings that are responsible for the Yellowstone Hotspot Track (Faccenna et al., 2010). James et al. (2011) calculated the combined convergence of the Farallon plate fragment and the North American continent to be approximately 4.4 cm/a since 16.5 Ma. This model is controversial as an origin for the CRBG and the Yellowstone hotspot (Camp, 2013); however, it is consistent with the geographically extensive mid-Miocene to Holocene volcanism throughout the SRP and is not necessarily mutually exclusive with deep mantle plume models.

Upwellings from the mantle asthenosphere are unlikely to be the direct source for the SMB and SRP basalts in this study as they do not have the low $^{87}Sr/^{86}Sr$ (<0.7030) one would expect from that source. Nor does the isotopic composition of these basalts have a typical OIB like signature (Weaver, 1991), so these basalts are not the result of remobilized subducted lithosphere. Rather, this upwelling mantle may conductively heat subcontinental lithosphere or, perhaps, induce delamination and partial melting of subcontinental lithosphere (Camp and Hanan, 2008), or result in ductile gravitational instabilities leading to adiabatic melting (Elkins-Tanton, 2007).

SRP Tectonic Model

Backtracking the leading edge of the Farallon slab fragment imaged by James et al. (2011) to 10 Ma places the leading edge of the slab fragment approximately 40 km southwest of Twin Falls approaching the confluence of the WSRP and ESRP (Figure 1.9). As the slab fragment moved from there to its present position, the northwest edge of the slab would be approximately 110 km southeast of Boise. We hypothesize that in the past, as now, focused mantle upwellings were generated along the leading and northwest edges of the slab fragment. Beneath the WSRP these upwellings

encountered thinned lithosphere due to extension, resulting in basaltic volcanism. After the passage of the leading edge of the slab, lateral flow around the upwardly angled northwestern edge of the slab fragment continued to generate mantle upwellings, waning at approximately 7 Ma. As suggested by James et al. (2011) continued mantle upwellings around the northwestern edge of the slab fragment resulted in pulses of basaltic volcanism throughout the central and ESRP. Just as basaltic volcanism continues into the Holocene in the ESRP, the upwellings periodically induced pulses of volcanism in the WSRP including the 2.2 - 0.9 Ma M2 basalts.

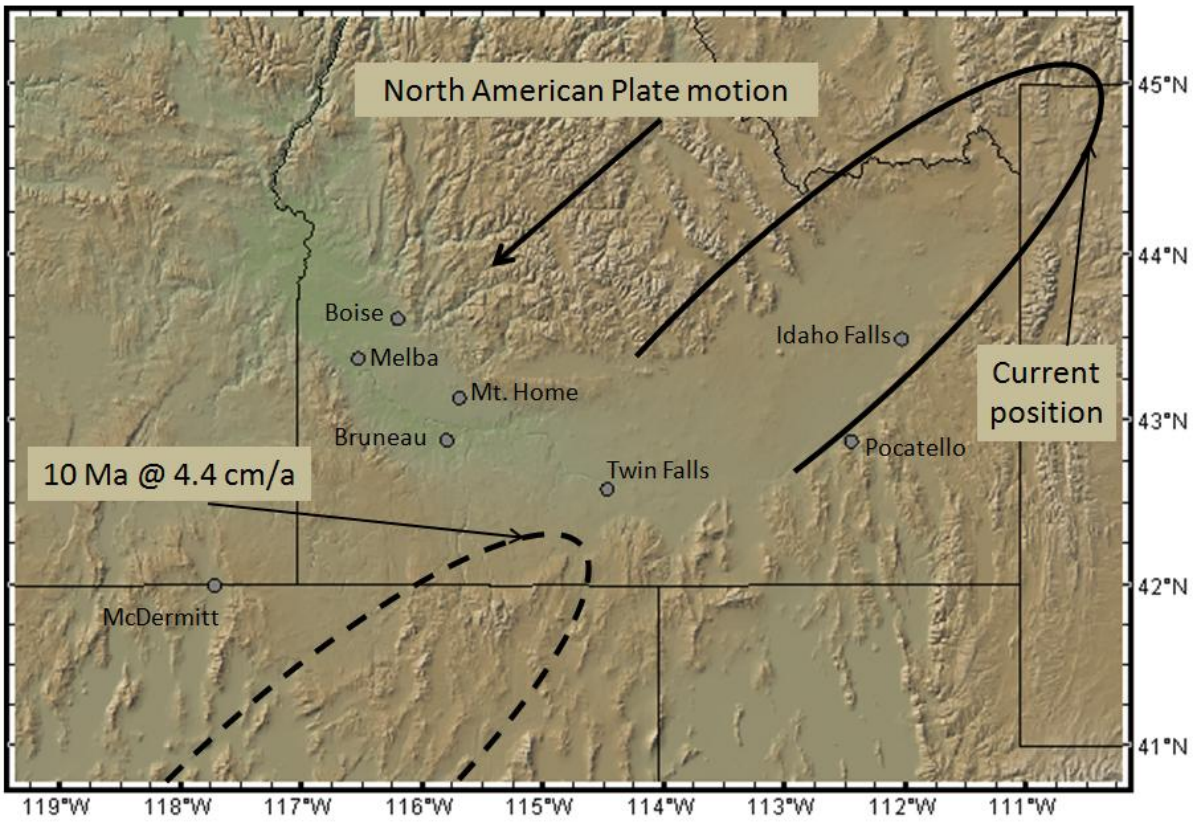

Figure 1.9. Slab fragment model for the Snake River Plain. Solid ellipse indicates approximate surface projection of a slab fragment imaged at 400 km depth generating a sheet-like upwelling along its northwest edge (James et al., 2011); though not shown, the slab fragment extends southwest to approximately the Idaho-Nevada border. Dashed ellipse indicates approximate location of the slab fragment at 10 Ma assuming relative velocity of 4.4 cm/a as calculated by James et al. (2011). Figure generated with GeoMapApp, http://www.geomapapp.org (Ryan et al., 2009).

Saddle Mountains Tectonic Model

Xue and Allen (2007) imaged the Juan de Fuca slab dipping 50° under western Oregon and Washington. They found that the leading edge of the plate is at approximately 400 km depth. They propose that the impinging Yellowstone plume head was trapped under the subducting plate at approximately 20 Ma (Geist and Richards, 1993) until it broke through at approximately 17 Ma. This suggests that slab fragments below, and to the northeast, of the break would generate focused mantle upwellings as proposed by Facenna et al. (2010). As these slab fragments approached the transition zone the upwellings generated would become more vigorous (Faccenna et al., 2010), generating the Saddle Mountain basalts from subcontinental lithosphere common to the SRP basalts in this study.

CONCLUSION

WSRP basaltic volcanism has had a common source for at least the period from ≥11 to 1 Ma (White et al., 2002), which is indistinguishable from the mantle source that generated much of the Saddle Mountain basalt of the CRBG. We suggest that the basaltic volcanism of the WSRP from 9-7 Ma was caused by focused mantle upwelling generated by the edge of the subducted Farallon plate, which approached the confluence of the WSRP and ESRP at 10 Ma (James et al., 2011). This upwelling encountered thinned lithosphere under the WSRP due to previous extension, resulting in increased basaltic volcanism starting at 9 Ma. Because the leading edge of the slab fragment passed to the northeast, volcanism waned in this location after 7 Ma. Later, at 2.2 Ma, upwelling around the northwest edge of the slab fragment lead to generation of the M2 basalts; despite the hiatus, these younger lavas derive from the same subcontinental lithospheric source. Many of the 13 to 8.5 Ma Saddle Mountain basalts that erupted from vents ~400 km away also came from a mantle source that is very different from that of the older Columbia River basalts but is compositionally indistinguishable from the WSRP basalts and many ESRP basalts. The eruption of the SMB may be due to the same focused mantle upwellings generated by the fragmentation of the Juan de Fuca plate

at approximately 17 Ma (Xue and Allen, 2007). The tomographic images of James et al. (2011), Xue and Allen (2007), and others (Li et al., 2008; Smith et al., 2009; Obrebski et al., 2010) suggest that the origin of these mantle upwellings starts at approximately 400 km depth and possibly extends down through the mantle transition zone. We emphasize that the implications of this model have little or nothing to do with the origin of the main phases of the Columbia River Basalts and do not provide any evidence for or against the proposed Yellowstone plume.

REFERENCES

Armstrong, R.I., Leeman, W.P., and Malde, H.E., 1975. K-Ar dating, Quaternary and Neogene volcanic rocks of the Snake River Plain, Idaho: American Journal of Science, v. 275, no. 3, p. 225-251.

Bailey, D.G., and Conrey, R. M., 1992. Common parent magma for Miocene to Holocene mafic volcanism in the northwestern United States: Geology, v. 20, no.12, p. 1131-1134.

Barry, T.L., Kelley, S.P., Reidel, S.P., Camp, V.E., Self, S., Jarboe, N.A., Duncan, R.A., and Renne, P.R., 2013. Eruption chronology of the Columbia River Basalt Group: Geological Society of America Special Paper 497, p. 45-66.

Braile, L.W., Smith, R.B., Ansorge, J., Baker, M.R., Sparlin, M.A., Prodehl, C., Schilly, M.M., Healy, J.H., St. Mueller, and Olsen, K.H., 1982. The Yellowstone-Snake River Plain seismic profiling experiment: Crustal structure of the eastern Snake River Plain: Journal of Geophysical Research: Solid Earth (1978-2012), v. 87, no. B4, p. 2597-2609.

Camp, V.E., 2013. Origin of Columbia River Basalt: Passive rise of shallow mantle, or active upwelling of a deep-mantle plume?: Geological Society of America Special Papers, v. 497, p. 181-199.

Camp, V.E., and Hanan, B.B., 2008. A plume-triggered delamination origin for the Columbia River Basalt Group: Geosphere, v. 4, no. 3, p. 480-495.

Carlson, R.W., Lugmair, G.W., and Macdougall, J.D., 1981. Columbia River volcanism: The question of mantle heterogeneity or crustal contamination: Geochimica et Cosmochimica Acta, v. 45, p. 2483-2499.

Carlson, R.W., 1984. Isotopic constraints on Columbia River flood basalt genesis and the nature of the subcontinental mantle: Geochimica et Cosmochimica Acta, v. 48, p. 2357-2372.

Christiansen, R.L., Foulger, G.R., and Evans, J.R., 2002. Upper-mantle origin of the Yellowstone hotspot: Geological Society of America Bulletin, v. 114, p. 1245-1256.

Church, S.E., 1976. The Cascade Mountains revisited: A re-evaluation in light of new lead isotopic data: Earth and Planetary Science Letters, v. 29, no. 1, p. 175-188.

Clemens, D.M., 1993, Tectonics and silicic volcanic stratigraphy of the western Snake River Plain, Idaho: Arizona State University M.S. thesis, 209 pages.

Coble, M.A., and Mahood, G.A., 2012. Initial impingement of the Yellowstone plume located by widespread silicic volcanism contemporaneous with Columbia River flood basalts: Geology, v. 40, no. 7, p. 655-658.

Elkins-Tanton, L.T., 2007. Continental magmatism, volatile recycling, and a heterogeneous mantle caused by lithospheric gravitational instabilities: Journal of Geophysical Research: Solid Earth, v. 112, no. B3.

Faccenna, C., Becker, T.W., Lallemand, S., Lagabrielle, Y., Funiciello, F., and Piromallo, C., 2010. Subduction-triggered magmatic pulses: A new class of plumes? Earth and Planetary Science Letters, v. 299, p. 54-68.

Geist, D., and Richards, M., 1993. Origin of the Columbia Plateau and Snake River plain — deflection of the Yellowstone plume: Geology, v. 21, p. 789-792.

GeoMapApp. http://www.geomapapp.org

GERM. Geochemical Earth Reference Model. http://earthref.org/GERM/

Ghiorso, Mark S., and Sack, Richard O., 1995. Chemical Mass Transfer in Magmatic Processes. IV. A Revised and Internally Consistent Thermodynamic Model for the Interpolation and Extrapolation of Liquid-Solid Equilibria in Magmatic Systems at Elevated Temperatures and Pressures: Contributions to Mineralogy and Petrology, v. 119, no. 2-3, p. 197-212.

Hanson-Hedgecock, S., Wagner, L.S., Fouch, M.J., and James, D.E., 2012. Constraints on the causes of mid-Miocene volcanism in the Pacific Northwest US from ambient noise tomography: Geophysical Research Letters, v. 39, no. 5.

Helz, R.T., 1978. The Petrogenesis of the Ice Harbor Member, Columbia Plateau, Washington – A chemical and experimental study [Ph.D. thesis]: University Park, Pennsylvania State University, 284 pages.

Honjo, N., 1986. Petrology and geochemistry of the Magic Reservoir eruptive center, Snake River Plain, Idaho: M.S. thesis, Rice University, 1986.

Hooper, P.R., 1984. Physical and chemical constraints on the evolution of the Columbia River basalt: Geology, v. 12, p. 495-499.

Hooper, P. R., 1997. The Columbia River flood basalt province: Current status, in Large Igneous Provinces: Continental, Oceanic, and Planetary Flood Volcanism, Geophysical Monograph 100, edited by J. Mahoney and F. Coffin, p. 1-27, AGU, Washington, D. C.

Hooper, P.R., 2000. Chemical discrimination of Columbia River basalt flows: Geochemistry, Geophysics, Geosystems, v. 1, no. 6.

Hooper, P.R., and Hawkesworth, C.J., 1993. Isotopic and Geochemical Constraints on the Origin and Evolution of the Columbia River Basalt: Journal of Petrology, v. 34, no. 6, p. 1203-1246.

Hooper, P.R., Johnson, J., and Hawkesworth, C.J., 2002. A model for the origin of the western Snake River Plain as an extensional strike-slip duplex, Idaho and Oregon, in Bill Bonnichsen, C.M. White, and Michael McCurry, eds., Tectonic and Magmatic Evolution of the Snake River Plain Volcanic Province: Idaho Geological Survey Bulletin, v. 30, p. 59-67.

Hooper, P.R., and Swanson, D.A., 1990. The Columbia River Basalt Group and associated volcanic rocks of the Blue Mountains province, chap. 4, of Geology of the Blue Mountains region of Oregon, Idaho, and Washington: Cenozoic Geology of the Blue Mountains Region, US Geological Survey Professional Paper 1437, p. 63-100.

Hughes, S.S., McCurry, M., and Geist, D.J., 2002. Geochemical correlations and implications for the magmatic evolution of basalt flow groups at the Idaho National Engineering and Environmental Laboratory: Geological Society of America Special Paper 353, p. 151-173.

James, D.E., Fouch, M.J., Carlson, R.W., and Roth, J.B., 2011. Slab fragmentation, edge flow and the origin of the Yellowstone hotspot track: Earth and Planetary Science Letters, v. 311, no. 1, p. 124-135.

Jarboe, N.A., Coe, R.S., Renne, P.R., Glen, J.M.G., and Mankinen, E.A., 2008. Quickly erupted volcanic sections of the Steens Basalt, Columbia River Basalt Group: secular variation, tectonic rotation, and the Steens Mountain reversal: Geochemistry, Geophysics, Geosystems, v. 9, no. 11.
Jarboe, N.A., Coe, R.S., Renne, P.R., and Glen, J.M.G., 2010. The age of the Steens reversal and the Columbia River Basalt Group. Chemical Geology, v. 274, no. 3, p. 158–168.

Kauffman, J.D., 2007. Major Oxide and Trace Element Analyses for Volcanic Rock Samples from Idaho, 2004-2005: Idaho Geological Survey Digital Analytical Data (DAD-4).

King, S.D., and Anderson, D.L., 1995. An alternative mechanism of flood basalt formation: Earth and Planetary Science Letters, v. 136, no. 3, p. 269-279.

Knobel, L.L., Cecil, L.D., and Wood, T.R., 1995. Chemical composition of selected core samples, Idaho National Engineering Laboratory, Idaho: No. DOE/ID--22126; USGS-OFR--95-748, Geological Survey, Idaho Falls, ID.

Kuntz, M.A., Covington, H.R., and Schorr, L.J., 1992. An overview of basaltic volcanism of the eastern Snake River Plain, Idaho, in: Regional Geology of Eastern Idaho and Western Wyoming: Geological Society of America Memoir, v. 179, p. 227-267.

Leeman, W.P., and Vitaliano, C.J., 1976. Petrology of McKinney Basalt, Snake River Plain, Idaho: Geological Society of America Bulletin, v. 87, no. 12, p. 1777-1792.

Li, C., van der Hilst, R.D., Engdahl, E.R., and Burdick, S., 2008. A new global model for P wave speed variations in Earth's mantle: Geochemistry, Geophysics, Geosystems, v. 9, no. 5.

Long, M.D., Till, C.B., Druken, K.A., Carlson, R.W., Wagner, L.S., Fouch, M.J., James, D.E., Grove, T.L., Schmerr, N., and Kincaid, C., 2012. Mantle dynamics beneath the Pacific Northwest and the generation of voluminous back-arc volcanism: Geochemistry, Geophysics, Geosystems, v. 13, no. 8.

Lum, C.C.L, Leeman, W.P., Foland, K.A., Kargel, J.A., and Fitton, J.D., 1989. Isotopic Variations in Continental Basaltic Lavas as Indicators of Mantle Heterogeneity: Examples From the Western U.S. Cordillera: Journal of Geophysical Research: Solid Earth (1978-2012), v. 94, no. B6, p. 7871-7884.

Mabey, D.R., 1976. Interpretation of a gravity profile across the western Snake River Plain, Idaho: Geology, v. 4, no. 1, p. 53-55.

Mabey, D.R., 1982. Geophysics and tectonics of the Snake River Plain, Idaho: in: Bill Bonnichsen and R.M. Breckenridge, (eds.), Cenozoic Geology of Idaho: Idaho Bureau of Mines and Geology Bulletin, v. 26, p. 139-154.

McDougall, I., 1976. Geochemistry and origin of basalt of the Columbia River Group, Oregon and Washington: Geological Society of America Bulletin, v. 87, no. 5, p. 777-792.

McQuarrie, N., and Rodgers, D.W., 1998. Subsidence of a volcanic basin by flexure and lower crustal flow: The eastern Snake River Plain, Idaho: Tectonics, v. 17, no.2, p. 203-220.

Morgan, W.J., 1972. Deep mantle convection plumes and plate motions: The American Association of Petroleum Geologists Bulletin, v. 56, no. 2, p. 203-213.

Nelson, D.O., 1980. Strontium isotopic and trace element geochemistry of the Saddle Mountains and Grande Ronde Basalts of the Columbia River Basalt group: Ph.D. Thesis, Oregon State Univ., Corvallis.

Obrebski, M., Allen, R.M., Xue, M., and Hung, S.H., 2010. Slab-plume interaction beneath the Pacific Northwest: Geophysical Research Letters, v. 37, no. 14.

Pierce, K.L., and Morgan, L.A., 1992. The track of the Yellowstone hotspot: volcanism, faulting, and uplift: in: Link, P.K., Kuntz, M.A., and Piatt, L.B., (eds.), Regional Geology of Eastern Idaho and Western Wyoming: Geological Society of America Memoir, v. 179, p. 1-53.

Pierce, K.L., and Morgan, L.A., 2009. Is the track of the Yellowstone hotspot driven by a deep mantle plume? — Review of volcanism, faulting, and uplift in light of new data: Journal of Volcanology and Geothermal Research, v. 188, no. 1, p. 1-25.

Reidel, S.P., Camp, V.E., Tolan, T.L., and Martin, B.S., 2013. The Columbia River flood basalt province: Stratigraphy, areal extent, volume, and physical volcanology. Geological Society of America Special Paper 497, p. 1-43.

Rodgers, D.W., Ore, H.T., Bobo, R.T., McQuarrie, N., and Zentner, N., 2002. Extension and subsidence of the eastern Snake River Plain, Idaho: in: Bill Bonnichsen, C.M. White, and Michael McCurry, (eds.), Tectonic and Magmatic Evolution of the Snake River Plain Volcanic Province: Idaho Geological Survey Bulletin, v. 30, p. 121-155.

Ryan, W.B.F., Carbotte, S.M., Coplan, J.O., O'Hara, S., Melkonian, A., Arko, R., Weissel, R.A., Ferrini, V., Goodwillie, A., Nitsche, F., Bonczkowski, J., and Zemsky, R., 2009. Global Multi-Resolution Topography synthesis: Geochemistry, Geophysics, Geosystems, v. 10, no. 3.

Shaw, D.M., 1970. Trace element fractionation during anatexis: Geochimica et Cosmochimica Acta, v. 34, no. 2, p. 237-243.

Shervais, J.W., and Hanan B.B., 2008. Lithospheric topography, tilted plumes, and the track of the Snake River-Yellowstone hot spot: Tectonics, v. 27, no. 5.

Shervais, J.W., Schroff, G., Vetter, S.K., Matthews, S., Hanan, B.B., and McGee, J.J., 2002. Origin and evolution of the western Snake River Plain: Implications from stratigraphy, faulting, and the geochemistry of basalts near Mountain Home, Idaho: in: Bill Bonnichsen, C.M. White, and Michael McCurry, (eds.), Tectonic and Magmatic Evolution of the Snake River Plain Volcanic Province: Idaho Geological Survey Bulletin, v. 30, p. 343-361.

Shervais, J.W., Vetter, S.K., and Hanan, B.B., 2006. Layered mafic sill complex beneath the eastern Snake River Plain: Evidence from cyclic geochemical variations in basalt: Geology, v. 34, no. 5, p. 365-368.

Shervais, J.W., and Vetter, S.K., 2009. High-K alkali basalts of the Western Snake River Plain (Idaho): Abrupt transition from tholeiitic to mildly alkaline plume-derived basalts: Journal of Volcanology and Geothermal Research, v. 188, no. 1, p. 141–152.

Smith, R.B., Jordan, M., Steinberger, B., Puskas, C.M., Farrell, J., Waite, G.P., Husen, S., Chang, W., and O'Connell, R., 2009. Geodynamics of the Yellowstone hotspot and mantle plume: Seismic and GPS imaging, kinematics, and mantle flow: Journal of Volcanology and Geothermal Research, v. 188, no. 1, p. 26-56.

Swanson, D.A., Wright, T.L., Hooper, P.R., and Bentley, R.D., 1979. Revisions in Stratigraphic Nomenclature of the Columbia River Basalt Group: US Government Printing Office (Washington), 102-041-142.

Till, C.B., Grove, T.L., Carlson, R.W., Donnelly-Nolan, J.M., Fouch, M.J., Wagner, L.S., and Hart, W.K., 2013. Depths and temperatures of <10.5 Ma mantle melting and the lithosphere-asthenosphere boundary below southern Oregon and northern California: Geochemistry, Geophysics, Geosystems, v. 14, no. 4, p. 864-879.
Tolan, T.L., Reidel, S.P., Beeson, M.H., Anderson, J.L., Fecht, K.R., and Swanson, D.A., 1989. Revisions to the estimates of the areal extent and volume of the Columbia River Basalt Group: Geological Society of America Special Paper 239, p. 1-20.

USGS. Geochemistry of rock samples from the National Geochemical Database: US Geological Survey, Reston, VA.

Wagner, L.S., Forsyth, D.W., Fouch, M.J., and James, D.E., 2010. Detailed three-dimensional shear wave velocity structure of the northwestern United States from Rayleigh wave tomography: Earth and Planetary Science Letters, v. 299, no. 3, p. 273-284.

Wagner, L.S., Fouch, M.J., James, D.E., and Hanson-Hedgecock, S., 2012. Crust and upper mantle structure beneath the Pacific Northwest from joint inversions of ambient noise and earthquake data: Geochemistry, Geophysics, Geosystems, v. 13, no. 12.

Weaver, B.L., 1991. The origin of ocean island basalt end-member compositions: trace element and isotopic constraints: Earth and Planetary Science Letters, v. 104, no. 2, p. 381-397.

White, C.M., Hart, W.K., Bonnichsen, B., and Matthews, D., 2002. Geochemical and Sr-Isotopic Variations in Western Snake River Plain Basalts, Idaho: in: Bill Bonnichsen, C.M. White, and Michael McCurry, (eds.), Tectonic and Magmatic Evolution of the Snake River Plain Volcanic Province: Idaho Geological Survey Bulletin, v. 30, p. 329-342.

Wolff, J.A.**,** Ramos, F.C., Hart, G.L., Patterson, J.D., and Brandon, A.D., 2008. Columbia River flood basalts from a centralized crustal magmatic system: Nature Geoscience, v. 1, no. 3, p. 177-180.

Wood, S.H., and Clemens, D.M., 2002. Geologic and tectonic history of the western Snake River Plain, Idaho and Oregon: in: Bill Bonnichsen, C.M. White, and Michael McCurry, (eds.), Tectonic and Magmatic Evolution of the Snake River Plain Volcanic Province: Idaho Geological Survey Bulletin, v. 30, p. 69-103.

Xue, M., and Allen, R.M., 2007. The fate of the Juan de Fuca plate: Implications for a Yellowstone plume head: Earth and Planetary Science Letters, v. 264, no. 1, p. 266–276.

Chapter 2: Grande Ronde Basalt across the Kamiak Gap: the Gravity Model Revisited using Constraints from the DOE Butte Gap Monitoring Well

ABSTRACT

The primary aquifer for storage and transport of groundwater in the Palouse groundwater basin is the Grande Ronde basalt. Within the Palouse basin the northern community of Palouse is connected to the southern cities of Pullman and Moscow through the Kamiak Gap, a topographic opening between Kamiak Butte on the west and the Ringo and Angel Buttes on the east. Uncertainty in the hydrologic connection of the Grande Ronde basalt through the Kamiak Gap has adversely affected efforts to manage the regional groundwater system. Holom (2006) conducted gravity measurements across the Kamiak Gap and presented a geophysical model concluding that the Grande Ronde basalt is not continuous through the Kamiak Gap. However, Conrey et al. (2013) has published new test well data that we use to impose constraints on the interpretation of the gravity data published in Holom (2006). We propose a new geophysical model suggesting that the Grande Ronde basalts are indeed continuous through the Kamiak Gap with a net thickness in excess of 100 m. Thus, Kamiak Gap should not create a hydraulic barrier to north-south groundwater flow. However, we note that the surface drainage divide actually lies between Kamiak Gap and Palouse, in an area north of the gravity control of Holom (2006). If a basement uplift is associated with this stream divide, the Grande Ronde basalt might thin at that location, creating a hydraulic barrier. More gravity stations north of Kamiak gap are needed to resolve that question.

INTRODUCTION

The Palouse groundwater basin (Figure 2.1) is approximately 1500 km^2 in extent and serves as the main water supply for Washington communities of Pullman, Colfax, and Palouse and their environs as well as Moscow, Idaho and its environs (Holom, 2006). The primary aquifer is the Grande Ronde basalt and recent studies suggest that its water level has been declining at a rate of approximately 30 to 45 cm/annum for the last four decades (Owsley, 2003). To be successful, future aquifer recharge strategies will require knowledge of the extent and hydrologic continuity of the Grande Ronde basalts throughout the Palouse groundwater basin. To this end, Holom (2006) conducted a gravity survey (Figure 2.2) to ascertain the continuity of the Grande Ronde basalt through the Kamiak Gap between the cities of Palouse in the north and Pullman/Moscow to the south. The subsequent model produced by Holom (2006) suggested that the Grande Ronde is not continuous through the Kamiak Gap.

The stratigraphy of the Kamiak Gap (Figure 2.3) consists of a surface covering of loess and Bovill clays of the Latah Formation underlain by approximately 50 meter thick basalts of the Priest Rapids Member of the Wanapum Basalt (Holom, 2006; Conrey et al., 2013). Below the Wanapum basalts are approximately 40 meter thick sedimentary interbeds of the Latah Formation consisting of variable extents of clay, sand, and gravel; this formation is considered to be equivalent to the Vantage Member of the Ellensburg Formation located in central Washington (Holom, 2006; Conrey et al., 2013). Sandwiched between the Latah (Vantage) sedimentary interbed above, and the crystalline igneous granites and metamorphic quartzite basement rocks below, is a variable thickness of Grande Ronde basalt consisting of, at least, the R2 units of Meyer Ridge and Grouse Creek (Holom, 2006; Conrey et al., 2013).

Recently Conrey et al. (2013) has published data for a Department of Ecology (DOE) test well drilled in the Kamiak gap (Figure 2.3) that provides constraints for the thicknesses and elevations of the stratigraphic units in the Kamiak Gap. The stratigraphy of the DOE Butte Gap well, drilled at the

latitude of the southernmost east-west transect of the Holom (2006) study, is remarkably similar to the stratigraphy of the Palouse City #3 well drilled to the north of the Kamiak Gap (Conrey et al., 2013). This suggests that the tops of the Wanapum, Latah (Vantage) interbed, and Grande Ronde stratigraphic layers may be flat through the Kamiak Gap which leads to simplifying assumptions in a gravity model for the gap. The Holom (2006) gravity model interpretation relied upon seemingly random undulations in the tops of the Wanapum, Latah (Vantage) interbed, and Grande Ronde tops without supporting geologic evidence. We present a gravity model using the gravity survey data of Holom (2006) with geology constrained by the DOE Butte Gap and the Palouse City #3 wells.

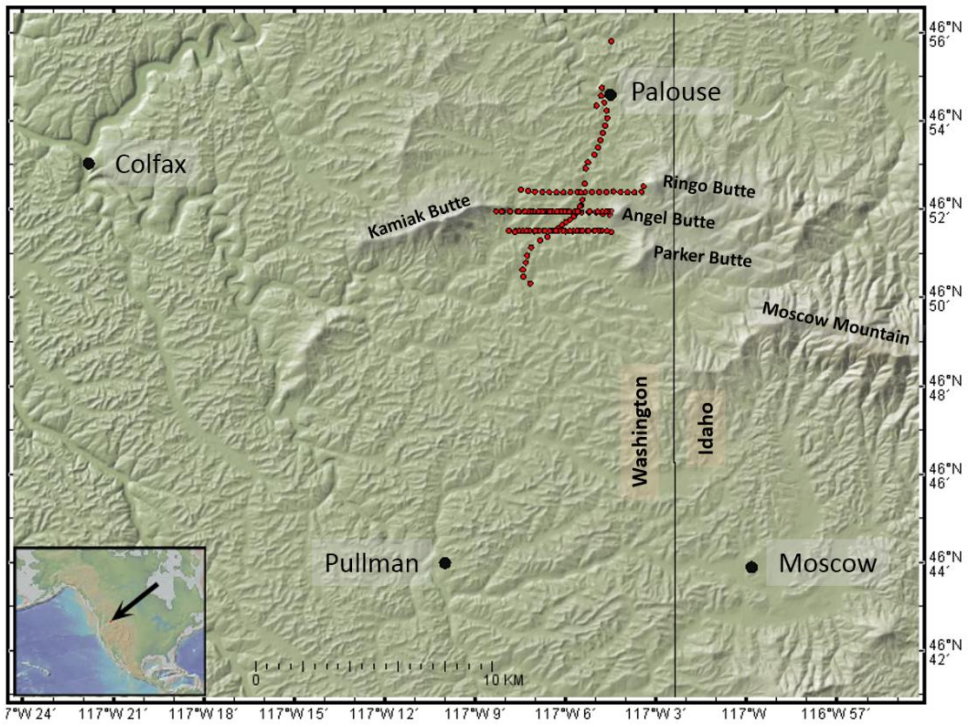

Figure 2.1. Area map of the Palouse groundwater basin. The red dots are the gravity survey points of Holom (2006) in the Kamiak Gap. Figure generated with GeoMapApp (Ryan et al., 2009).

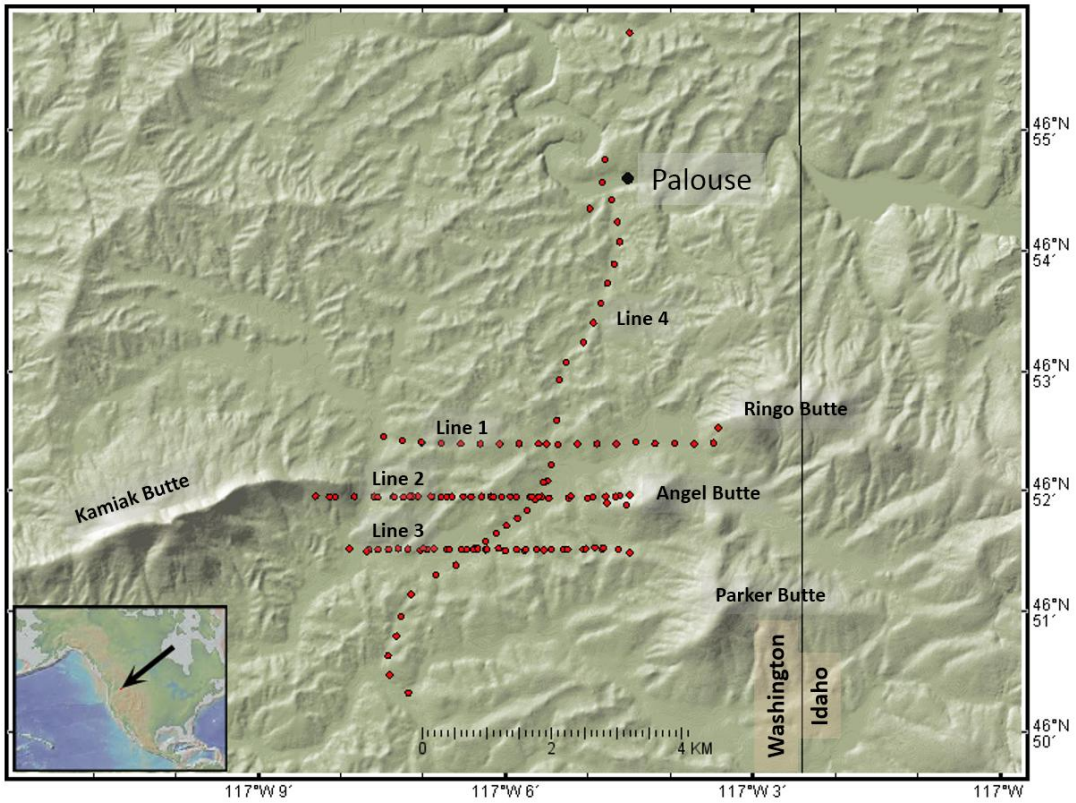

Figure 2.2. Blowup of gravity survey area in the Kamiak Gap. Lines 1, 2, and 3 are east-west transects across the gap and Line 4 meanders approximately north-south crossing the other three lines. The east end of Line 1 terminates in the bedrock of Ringo Butte. The western terminus of Line 2 is in the bedrock of Kamiak Butte whilst the eastern terminus is in the bedrock of Angel Butte. None of the other line termini are in bedrock. Figure generated with GeoMapApp (Ryan et al., 2009).

METHODOLOGY

Introduction

Holom (2006) conducted a gravity survey of 133 points in the Kamiak Gap (Figure 2.2). This included three east- west transects across the valley, designated Lines 1, 2, and 3 from north to south respectively, and one long meandering north-south transect, designated Line 4, crossing the three east-west transects. To avoid introducing new variables, our study presumes that the Holom (2006) procedures, from collection of raw data to removal of regional trend, are correct. We also use the same values for bulk densities of the various units present. However, we use stratigraphy from the

recently drilled DOE Butte Gap monitoring well, located in the Kamiak Gap at the latitude of Holom's (2006) Line 3, along with the stratigraphy of Palouse City #3 well to produce a new geophysical model, constraining the thicknesses of the subsurface beds above the Grande Ronde to be consistent with the two wells (Conrey et al., 2013). This last step, the simplest method of correlating the two wells, is in sharp contrast to the interpretation of Holom (2006) who invoked arbitrary and random variations in the Wanapum, Latah (Vantage) and soil thicknesses above the Grande Ronde, unsupported by any geological evidence, to force a fit between the gravity data and their interpretation of Grande Ronde thickness through the gap.

Figure 2.3 depicts the stratigraphy at two well sites; Pa #3 is Palouse City #3 well near the city of Palouse north of the Kamiak Gap, and Butte Gap is the DOE test well at the intersection of Line 3 and Line 4 in the Kamiak Gap (Conrey et al., 2013). The elevations of the respective beds is remarkably similar with the top of the Wanapum basalt at approximately 754 m MSL, the top of the Latah (Vantage) sediments at approximately 704 m MSL, and the top of the Grande Ronde basalt at approximately 662 m MSL. These elevations are used as simplifying constraints on the geophysical model throughout the Kamiak Gap and, barring more detailed knowledge of the regional geology, they are reasonable elevation assumptions. Admittedly, it seems to be a stretch to define the thickness of all of these beds based on well stratigraphy at only two points, but the extraordinary correlation of the stratigraphy of the two wells supports that assumption (at least through the central, deepest portion of the gap) for this simple model. With the thickness of the overlying loess sediments being determined by the difference in the elevation of the top of the Wanapum basalt (754 m MSL) and the measured surface elevation at each gravity survey point, the only remaining variable in the gravity model is the thickness of the Grande Ronde basalt down to basement. Our models use the same density values for the geologic units as used by Holom (2006).

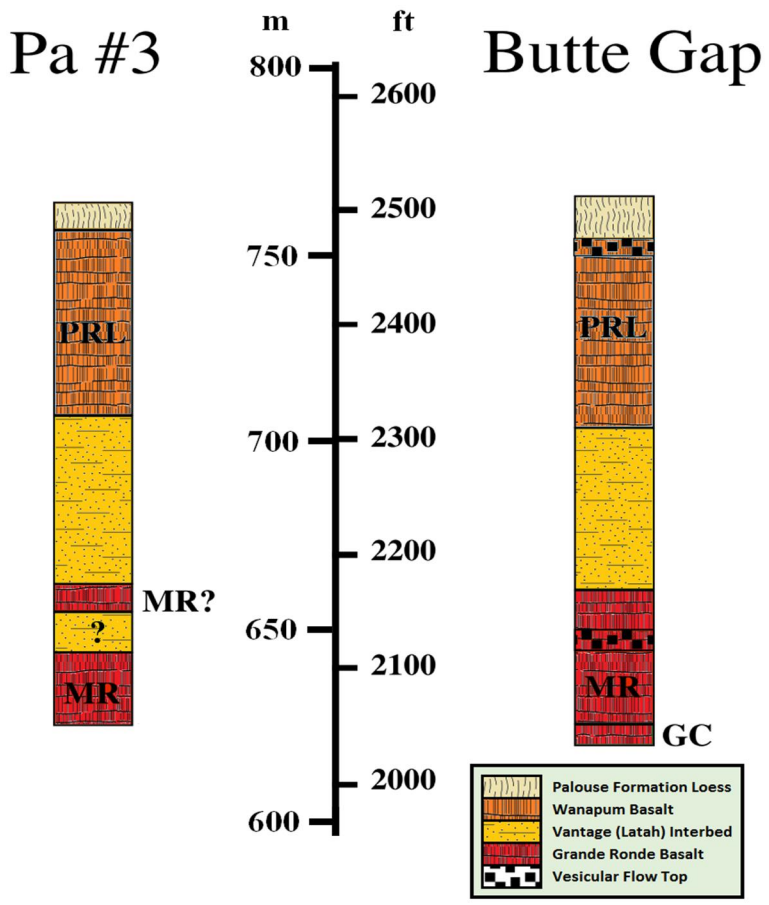

Figure 2.3. Well stratigraphy (modified from Conrey et al., 2013). Pa #3 is the Palouse City #3 well. Note its similarity to the DOE Butte Gap well as noted by Conrey et al. (2013). The top tan unit is soil (loess and Bovill clays). The checkered units are weathered vesicular basalt flow tops in both the Wanapum basalt and Grande Ronde basalt. PRL is the Priest Rapids Member of the Wanapum basalt, the yellow unit is the Latah (Vantage) interbed, mostly sand with variable gravel and clay. The lower red units are the Meyer Ridge and Grouse Creek units of the Grande Ronde R2. In both wells the top of the Wanapum Basalt is at approximately 754 m, the top of the Latah (Vantage) interbed is at approximately 704 m, and the top of the Meyer Ridge unit of the Grande Ronde at approximately 662 m.

Simple Bouguer Slab Model

First we analyze the stratigraphy found in the DOE Butte Gap well in terms of its bulk density and its effect on the gravity field. In this way we can isolate that part of the gravity anomaly that is due only to our target—the thickness of the Grande Ronde unit. We will call this reduced gravity the Grande Ronde anomaly. For example, if no Grande Ronde is present, the Grande Ronde anomaly

would be zero. If the Grande Ronde is present, the Grande Ronde anomaly would be negative (because the Grande Ronde has a negative density contrast compared to the surrounding country rock).

The new DOE Butte Gap monitoring well is at the intersection of Holom's Lines 3 and Line 4. This well provided the information we needed to correct the residual gravity for the flows and sediments above the Grande Ronde. The gravity attraction of a wide-spread horizontal geological unit of constant thickness can be calculated by the Bouguer slab formula:

$$\Delta gB = 2\,\pi\,G\rho\,h$$

where G is Newton's constant, ρ is the density contrast with the surrounding country rock, and h is the thickness of the unit. In convenient units this formula is

$$\Delta gB = 0.04189\,\rho\,h$$

where ρ is in g/cc and h is in meters and the result is in mGal. The Bouguer slab formula takes advantage of the fact that most of the gravity effect of an infinitely wide slab is due to the mass relatively close to the gravity measurement.

Next, we apply Holom's densities to the well log of the DOE Butte Gap well (Conrey et al., 2013). The gravity effect of each unit is shown in Figure 2.4 as calculated by the Bouguer slab formula. The total gravity effect of the units above the GR is -2.06 mGal. However, the residual gravity at this location is about -4.9 mGal, so there is a difference of -2.84 mGal of unexplained gravity anomaly at this location. We call this the Grande Ronde anomaly. Using the Bouguer slab formula, the thickness of the Grande Ronde at this location must be at least 251 m. The well penetrated 43 m of Grande Ronde before drilling stopped.

For our conceptual model and using Holom densities, the Grande Ronde Anomaly at any station is:

$$\Delta g = CBA - RT + 0.0595\,(Elev - 754) + 0.996$$

where CBA = Complete Bouguer Anomaly (mGal), RT = Regional Trend (mGal), and Elev = Gravity Station Elevation (m AMSL). Where Δg is positive, the Grande Ronde is absent and portions of the units above it have lapped on to crystalline basement rocks. Where Δg is negative, the Grande Ronde may exist.

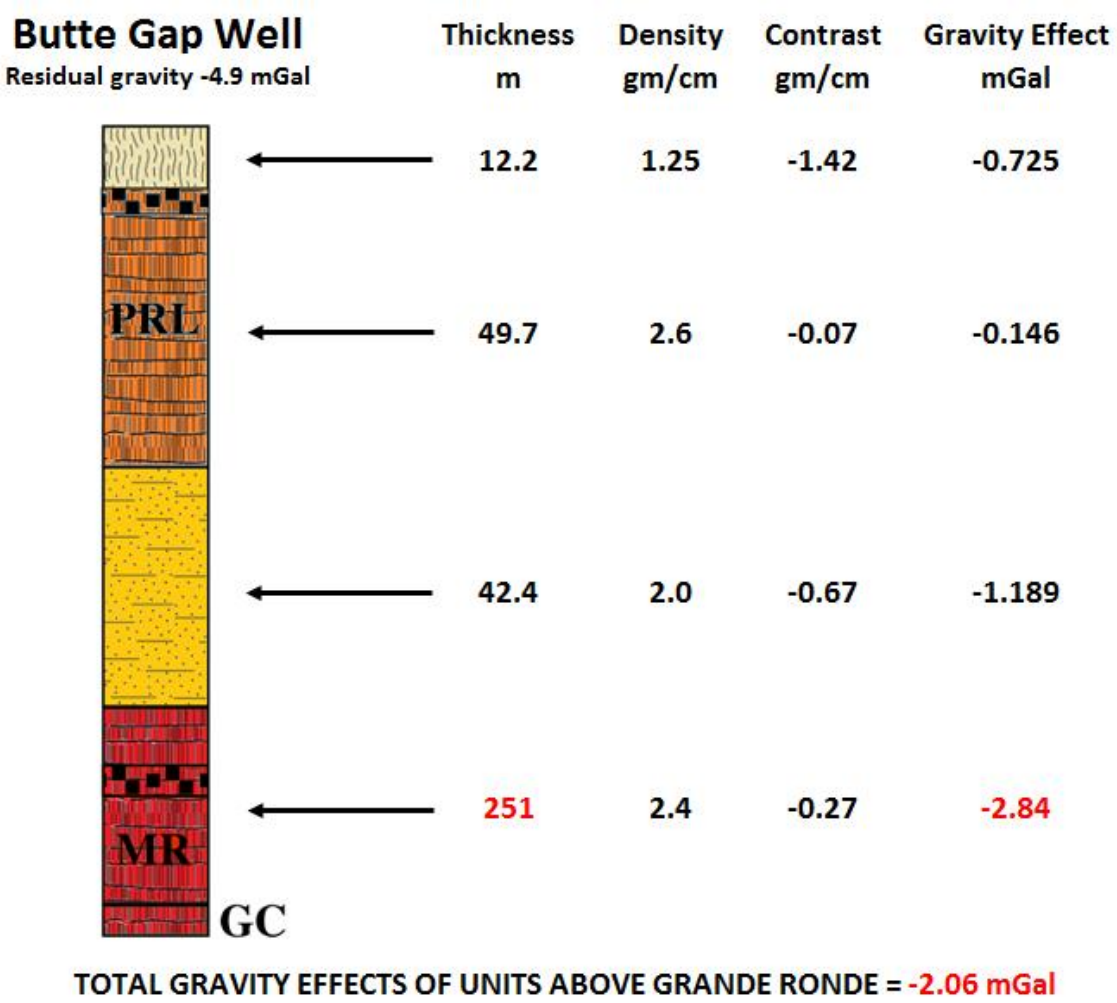

Figure 2.4. The bulk density, density contrast with respect to country rock, and gravity effect of each unit present in the DOE Butte Gap well. The stratigraphy above the Grande Ronde accounts for a net gravity effect of -2.06 mGal. See Figure 2.3 for description of units.

The map of the Grande Ronde anomaly (Figure 2.5) shows the gravity effect of the Grande Ronde unit in the Kamiak Gap, after correction for the thicknesses of loess, Wanapum, and Latah (Vantage) units as observed in the DOE Butte Gap and Palouse City #3 wells. Grande Ronde basalt can exist only within the 0 contours. Outside this boundary, the Grande Ronde anomaly is positive indicating that basement surface has risen above the 662 m AMSL level found in the DOE Butte Gap well. Note that the Grande Ronde anomaly is negative continuously across the gap indicating that the Grande Ronde unit is present. This is in contrast to Holom's interpretation of a barrier at Line 1. The red dots on Figure 2.5 are the gravity stations observed by Holom (2006). Had another east-west line of gravity observations been made north of Line 1 in the vicinity of the surface drainage divide (dashed line, Figure 2.5), we would be much more confident of the continuity of the Grande Ronde unit to the north of the Kamiak gap across the drainage divide. The question mark on Figure 2.5 indicates the area where more gravity station control is needed to resolve this question.

The minimum thickness H of the Grande Ronde unit near the center of the gap can be estimated using the Bouguer slab formula:

$$H = -\Delta g / 2 \pi\rho G = -88.4 \Delta g$$

where H is in meters, Δg is the Grande Ronde anomaly in mGal, and ρ is the density contrast between the Grande Ronde unit and the surrounding basement rocks (-0.27 g/cc). A map of this minimum thickness through the Kamiak gap (Figure 2.6) shows that the Grande Ronde thins across the gap toward the north but remains at least 120 m thick at its thinnest point on Line 1. Once again, this refutes Holom's (2006) interpretation which shows no Grande Ronde at all on Line 1. Thus the gravity data suggests that the Grande Ronde is continuous through the gap with sufficient thickness for groundwater flow. However, Figure 2.6 clearly shows that considerable uncertainty exists for the continuity of the Grande Ronde across the drainage divide north of the Kamiak gap. As with Figure 2.5, the question mark on Figure 2.6 indicates the area where more gravity stations are needed.

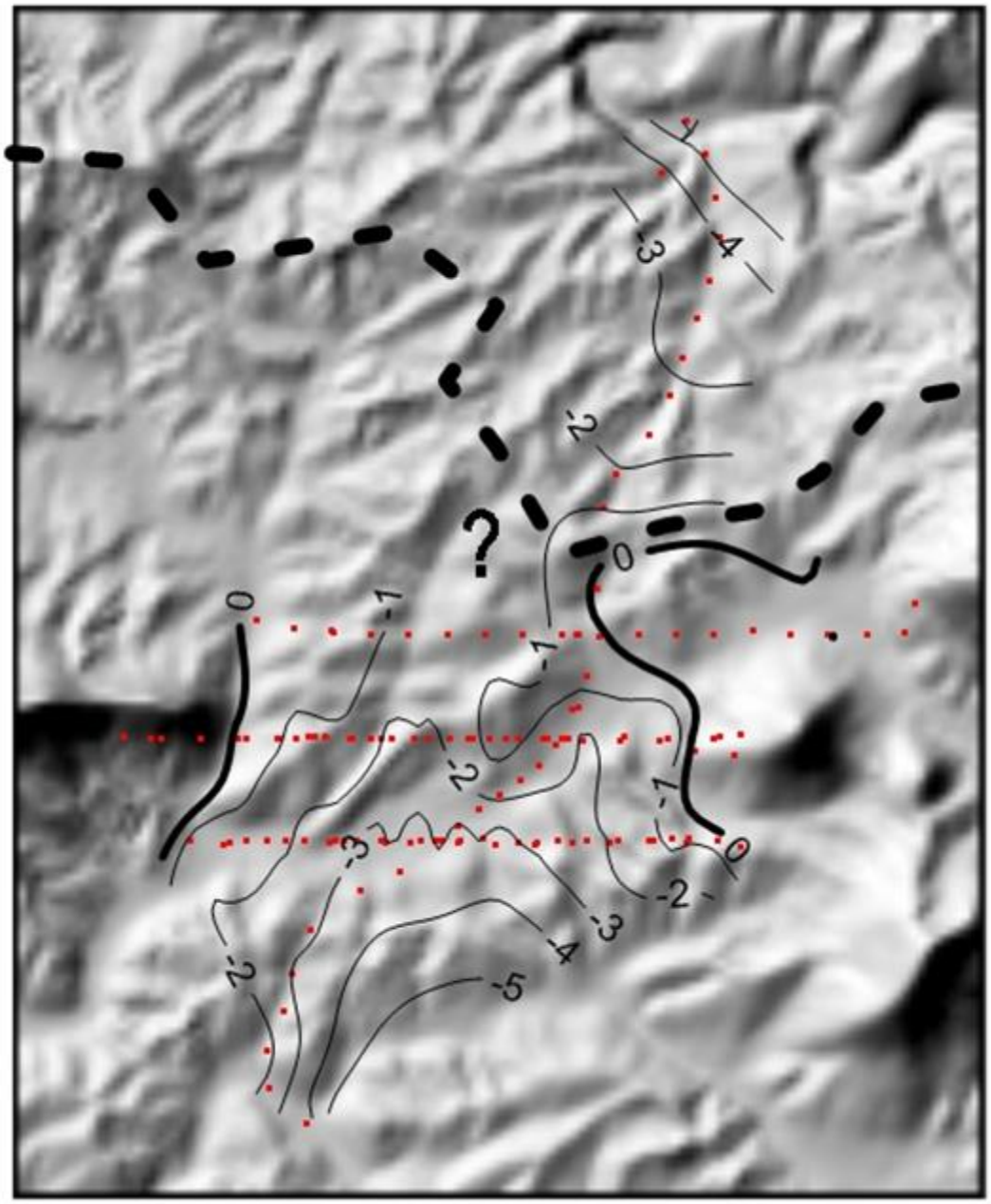

Figure 2.5. Grande Ronde anomaly in mGals. Contour interval is 1 mGal. This map represents the gravity effect of the Grande Ronde unit in the Kamiak Gap, after correction for the thicknesses of loess, Wanapum, and Latah (Vantage) units as observed in the DOE Butte Gap and Palouse City #3 wells. The Grande Ronde is present if this anomaly is negative. The red dots are gravity stations observed by Holom (2006). The dashed line is the surface drainage divide. The question mark indicates the area where more gravity station control is needed.

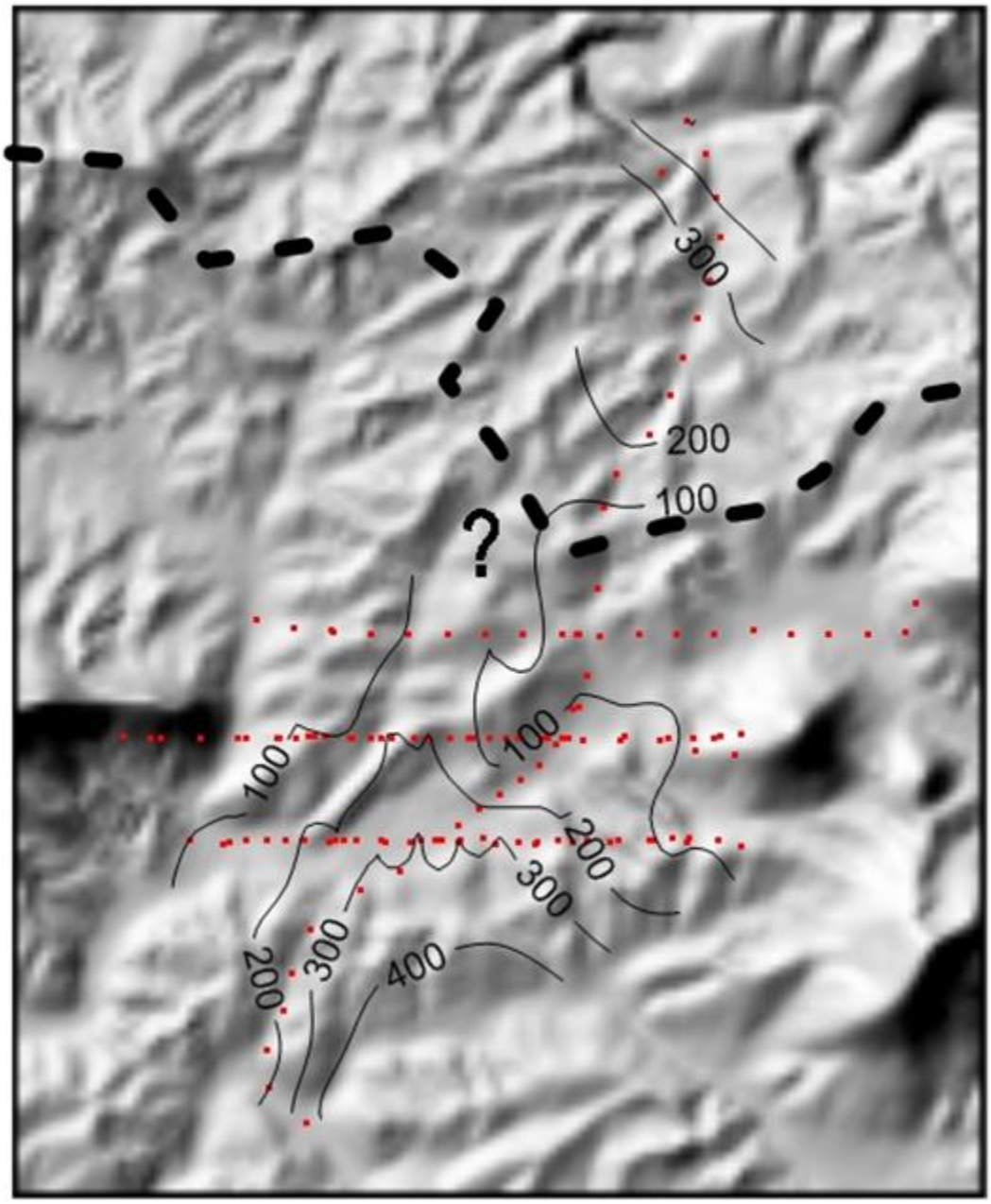

Figure 2.6. Minimum thickness in meters of the Grande Ronde unit across the Kamiak Gap. Contour interval = 100 m. This map is based on the simple Bouguer slab formula. It provides minimum thicknesses in the center of the gap but overestimates thicknesses near the edges. See the two-dimensional modeling results (Figures 2.7, 2.8, 2.9) for more accurate thickness estimates along the east-west gravity lines. The red dots are gravity stations observed by Holom (2006). The dashed line is the surface drainage divide. The question mark indicates the area where more gravity station control is needed.

Two-Dimensional Gravity Modeling

The Bouguer slab approximation described above is useful only to give a minimum thickness at the center of the gap. A better estimate of the actual Grande Ronde thickness can be obtained by two-dimensional gravity modeling. The three east-west gravity survey lines from Holom (2006) were processed for our model using the GravCad two-dimensional modeling program written by Steven D. Sheriff of the University of Montana. This program allows multiple polygons of designated densities to be depicted. The sinuous north-south Line 4, clearly not in a two-dimensional relationship to the geology, was processed only to ensure reasonable ties between the east-west lines. All lines were modeled using the density estimates of Holom (2006), with overlying loess from 754 m MSL to surface elevation with a density of 1.25 gm/cm^3, Wanapum basalt from 704 – 754 m MSL with a density of 2.60 gm/cm^3, Latah (Vantage) sediments from 662 – 704 m MSL with a density of 2.00 gm/cm^3. The Grande Ronde basalt density was modeled at 2.40 gm/cm^3 and the basement at 2.67 gm/cm^3.

In our modeling, our primary assumption was that the basement topography should change smoothly across the gap resulting in longer wavelength gravity anomalies. Thus we made no attempt to model local short wavelength changes in the gravity measurements from station to station. These local discrepancies are easily explained by nearby changes in soil density, thickness, or water content. Thus our modeled gravity lines are calculated to fit the overall shape of the gravity observations, which in turn, we assume to be representative of the overall basement shape.

DISCUSSION

Line 1

Holom (2006) concluded that Line 1 did not include Grande Ronde basalt and therefore the Grande Ronde aquifer was not continuous through the Kamiak Gap. However, as can be seen in Figure 2.7, our two-dimensional model suggests there is a significant channel of Grande Ronde basalt up to approximately 125 meters in thickness west of the Line 4 intersection. The westernmost point on Line 1 lies in a valley parallel to and less than 1 km north of the east-west trending ridge of Kamiak Butte. As Line 1 extends east towards the intersection of Line 4 it approaches the northern slopes of Angel Butte and continues on to terminate at the bedrock of Ringo Butte. Apparently, there is shallow crystalline bedrock in the vicinity of these two buttes.

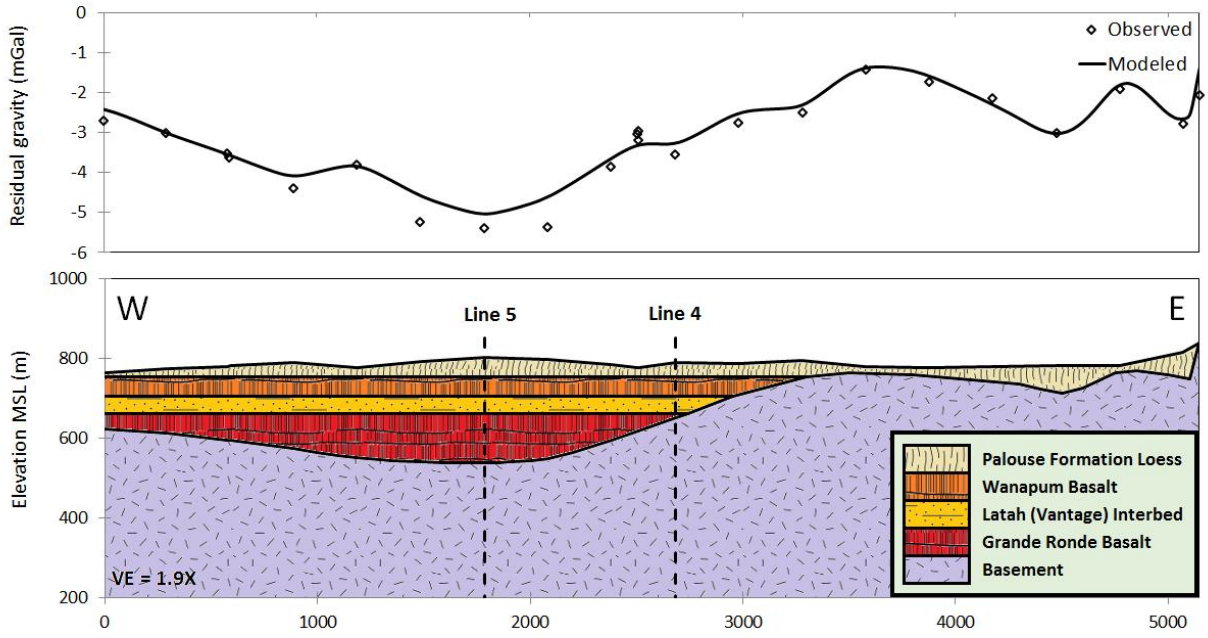

Figure 2.7. Gravity model of Line 1 (see Figure 2.2 for aerial view). The pattern and colors for stratigraphic units are depicted in legend at lower right; this same legend is used for all modeled lines in Figures 2.8, 2.9, 2.10, and 2.12. Maximum modeled thickness of Grande Ronde (Line 5) is 125 m; modeled thickness of Grande Ronde at intersection of Line 4 is 10 m.

Line 2

The bedrock of Kamiak Butte on the west and Angel Butte on the east demark the termini of Line 2 (Figure 2.8). Our model suggests that there is, again, a considerable extent of Grande Ronde basalt in a channel to the west of Line 4 to a thickness of approximately 224 meters at the latitude of Line 2. Line 4 appears to intersect with a shallower extent of Grande Ronde basalt (maximum thickness of approximately 175 m), however, based on the model for Line 1 it does not appear that this basalt extends far to the north but rather rapidly pinches out.

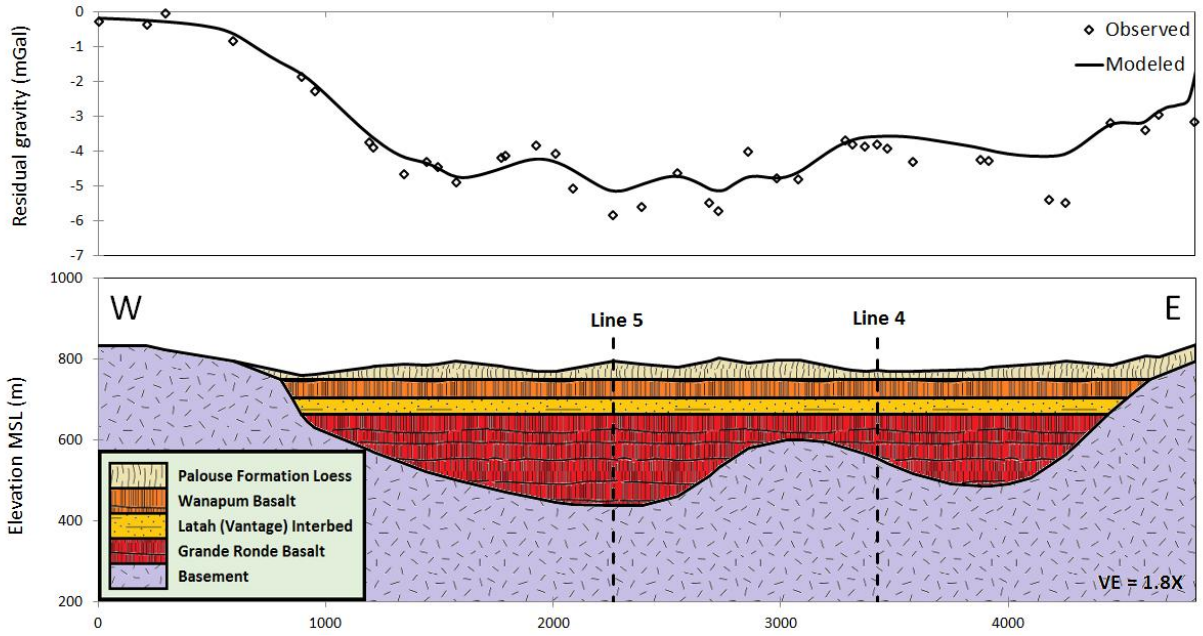

Figure 2.8. Gravity model of Line 2 (see Figure 2.2 for aerial view). Maximum modeled thickness of Grande Ronde (Line 5) is 224 m; modeled thickness of Grande Ronde at intersection of Line 4 is 107 m.

Line 3

The western terminus of Line 3 is slightly less than 1 km south of Kamiak Butte whilst the eastern terminus is slightly more than a half km south of Angel Butte (Figure 2.9). The extent of the Grande Ronde basalt channel has broadened and deepened considerably at this latitude with a maximum depth of approximately 316 meters, some 92 meters greater than 224 meter deep western channel modeled in Line 2.

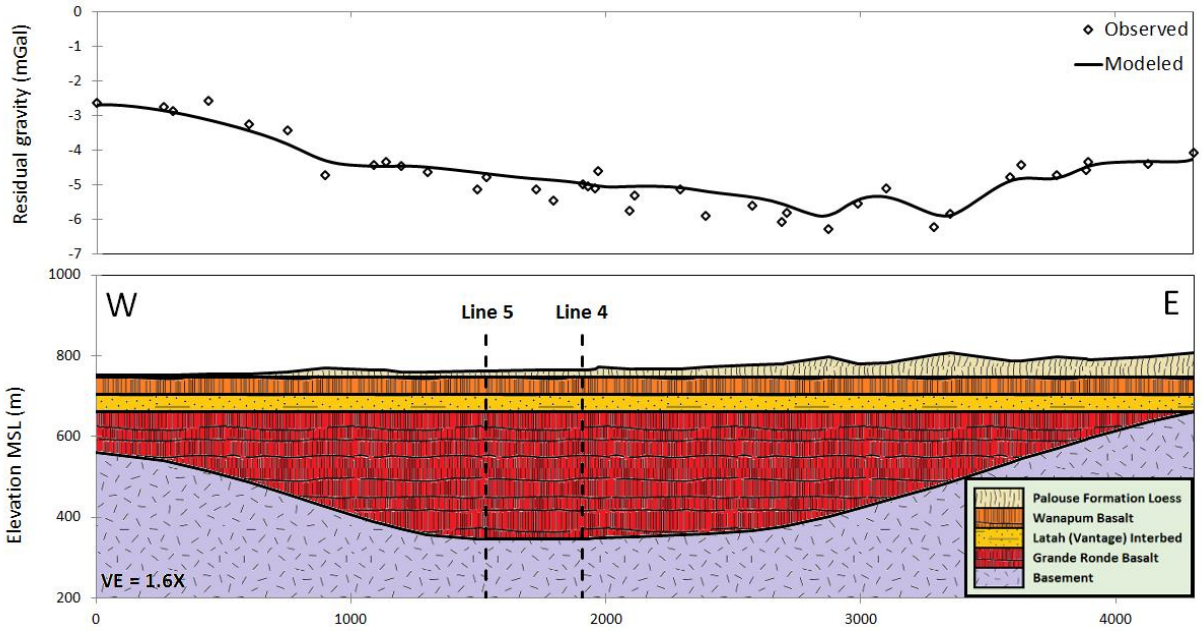

Figure 2.9. Gravity model of Line 3 (see Figure 2.2 for aerial view). Maximum modeled thickness of Grande Ronde (Line 5) is 316 m; modeled thickness of Grande Ronde at intersection of Line 4 is also 316 m.

Line 4

The model for Line 4 (Figure 2.10) suggests that the shallowest basement can be found slightly north of Line 1 (Figure 2.7). However, at the intersection of Line 4 with Lines 1 and 2, Line 4 is quite close to Angel Butte. As the models for Lines 1 and 2 suggest the deepest bedrock is slightly over 1 km west of Line 4 in a channel trending northeast-southwest. To the south at Line 3 the channel has broadened both east and west and Line 4 intersects Line 3 near the deepest bedrock (and thickest Grande Ronde basalt). By approximately a kilometer north of Line 1 the Line 4 model suggests that Grande Ronde basalt channel may also have broadened out east and west through the northern portion of the Kamiak Gap.

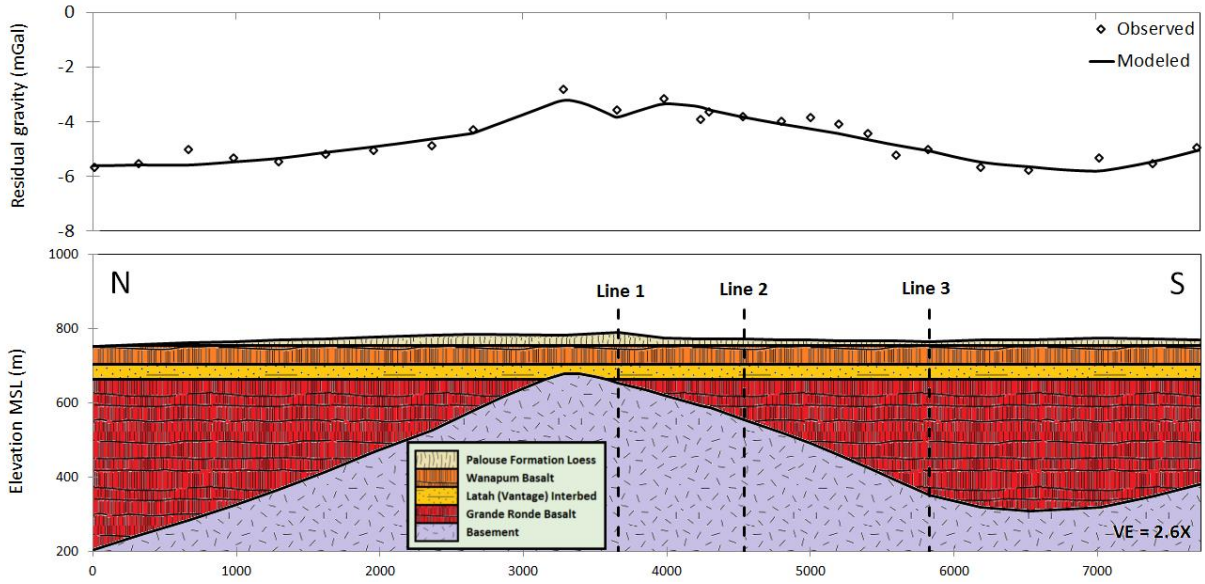

Figure 2.10. Gravity model of Line 4 (see Figure 2.2 for aerial view). Modeled thickness of Grande Ronde at intersection of Line 1 is 10 m, at intersection of Line 2 is 107 m, and at intersection of Line 3 is 316 m. Note that this line is sinuous and is not representative of the N-S structure of the valley. The basement high in the center of this section is, for example, considerably east of the center of the valley. See Figure 2.12 for a more representative N-S section.

Line 5

We have taken the northern and southern gravity survey points of Line 4 and extended them through the modeled Grande Ronde channel through the Kamiak Gap to the west of Line 4 (Figure 2.11) and the subsequent model is depicted in Figure 2.12. Unfortunately, there is approximately 1.35 km between the point modeled on Line 1 and closest point to the northeast on Line 4 (designated KMK043 and KMK112 respectively in Holom, 2006) leaving some uncertainty in the Grande Ronde thickness in the kilometer north of Line 1. However, our modeling of Lines 1 – 4 strongly suggest that there is a significant thickness of Grande Ronde in the western Kamiak Gap and, at least through the latitudes surveyed by Holom (2006), it is continuous.

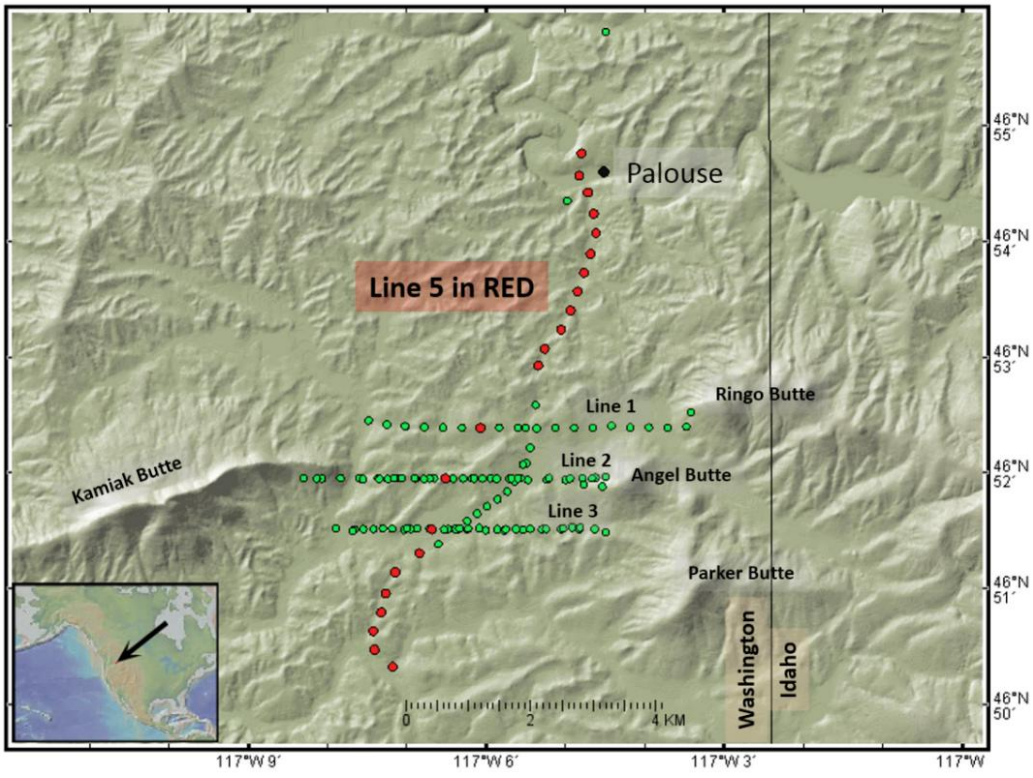

Figure 2.11. Aerial view of Line 5. The gravity survey points used to construct Line 5 are delineated in red. The three points in Lines 1, 2, and 3 are the points with the thickest Grande Ronde modeled in Figures 2.7, 2.8, and 2.9 respectively. Figure generated with GeoMapApp (Ryan et al., 2009).

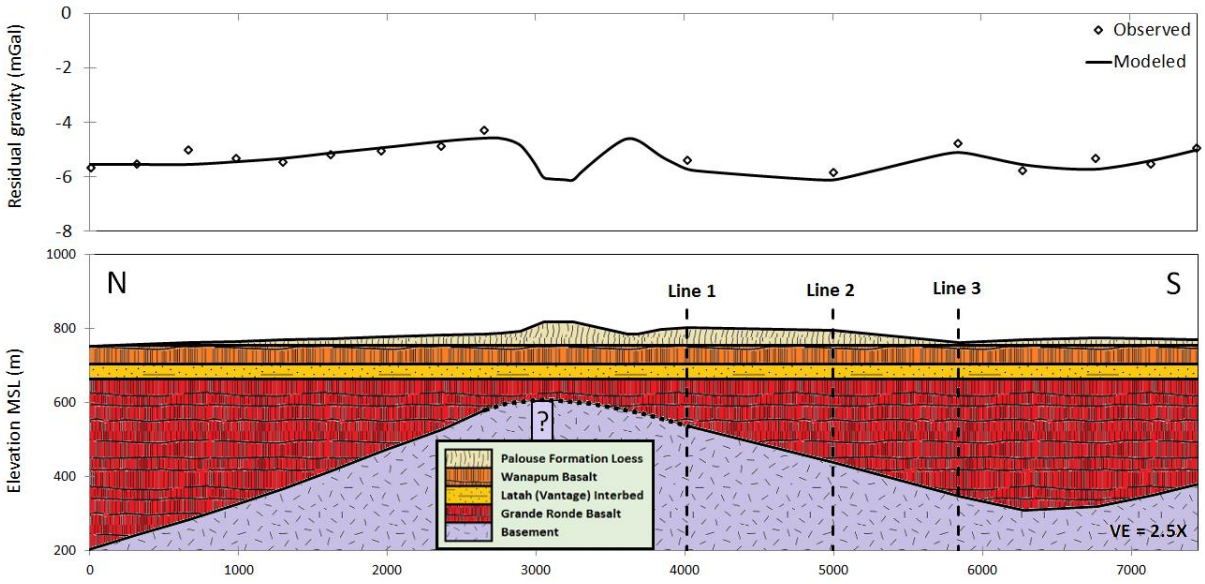

Figure 2.12. Gravity model of Line 5 (see Figure 2.11 for aerial view). This section is more representative of the N-S structure of the valley than Line 4. Modeled thickness of Grande Ronde at intersection of Line 1 is 125 m, at intersection of Line 2 is 224 m, and at intersection of Line 3 is 316 m. The dashed line between basement and Grande Ronde north of Line 1 below the topographic divide indicates uncertainty in the model as there is approximately 1.35 km between survey point locations.

CONCLUSION

This new geophysical model, using elevation constraints imposed by Palouse City #3 well and the DOE Butte Gap well, strongly suggests that there is a deep channel of Grande Ronde basalt running continuously north-south through the Kamiak Gap with a minimum thickness of near 125 m (at very least 120 m) at the latitude of Line 1. With this thickness available, it is reasonable to expect that the Grande Ronde aquifer hydrologically connects the north and south portions of the Palouse groundwater basin.

For purposes of discussion we define Kamiak Gap strictly as the area flanked by the Kamiak Butte on the west and the Ringo and Angel Buttes on the east. Unfortunately, Holom (2006) did not adequately survey the slightly higher elevation terrain immediately north of Kamiak Gap along the divide between the Palouse River and Fourmile Creek drainages (Figures 2.5-2.6). This surface

drainage divide lies between Kamiak Gap and Palouse, in an area north of the east-west gravity control lines of Holom (2006). Accordingly, Line 5 (Figure 2.12) indicates uncertainty for the Grande Ronde thickness immediately north of the latitude of Line 1 beneath the topographic divide. If a basement uplift is associated with the stream divide, the Grande Ronde might thin at that location, possibly creating a hydraulic barrier. Without further gravity measurements, this possibility cannot be ruled out. Thus, if future groundwater models do require a hydraulic barrier, it should be placed beneath the drainage divide, not in Kamiak Gap.

It is important to reiterate that our conclusions are based on exactly the same gravity observations, regional gravity trend, and bulk densities as used by Holom (2006). Our results are dramatically different because we used a much simpler (and far less subjective) stratigraphic model for the Latah (Vantage), Wanapum, and soil units above the Grande Ronde.

REFERENCES

Conrey, R., Beard, C., and Wolff, J., 2013. Columbia River Basalt flow stratigraphy in the Palouse Basin Department of Ecology test wells. Palouse Basin Aquifer Committee, http://www.webpages.uidaho.edu/pbac/

Holom, D., 2006. Ground water flow conditions related to the pre-basalt basement geometry delineated by gravity measurements near Kamiak Butte, eastern Washington. M.S. Thesis, University of Idaho.

Owsley, D., 2003. Characterization of Grande Ronde aquifers in the Palouse Basin using large scale aquifer tests. M.S. Thesis, University of Idaho.

Ryan, W.B.F., Carbotte, S.M., Coplan, J.O., O'Hara, S., Melkonian, A., Arko, R., Weissel, R.A., Ferrini, V., Goodwillie, A., Nitsche, F., Bonczkowski, J., and Zemsky, R., 2009. Global Multi-Resolution Topography synthesis: Geochemistry, Geophysics, Geosystems, v. 10, no. 3.

Chapter 3: Lunar Impact Structures and the Megaregolith: Insight from GRAIL Gravity and Crater Morphometry

ABSTRACT

The relationship between GRAIL gravity and lunar topography at short wavelengths can be explained by the impact structures visible on the present-day Moon surface. The currently visible craters represent only a small fraction of the impacts that have formed the thick lunar megaregolith since pre-Nectarian time. The brecciated and slumped materials associated with the currently visible craters form high porosity lenses bulked up compared to the adjoining heterogeneous megaregolith, resulting in negative gravity anomalies that are in phase with the topographic gravity signature. The currently visible craters on the Moon occur at many spatial scales, with an associated high porosity shock zone thickness inversely correlated with surface elevation. We show that the bulk density of megaregolith crust can be found from the GRAIL Bouguer reduction density only if the statistical relationship between the surface elevation and high porosity zone thickness of the currently visible crater structures is known. Using conventional crater geomorphometry models in conjunction with published GRAIL Bouguer reduction density and residual Bouguer anomaly results, we find that the average bulk density of the lunar megaregolith crust is 2225 kg/m^3, with a 95% confidence interval from 2163 to 2347 kg/m^3, much lower than the 2560 kg/m^3 commonly accepted. The high porosity zones associated with the currently visible craters are bulked up 4.8 % with a density contrast of -101 kg/m^3 compared to the surrounding megaregolith crust. The proportional scaling factor between the vertical extent of the high porosity zones and crater diameter is 1/6. The overall thickness of the megaregolith crust is 18 km.

INTRODUCTION

The currently visible craters on the lunar highlands essentially form the topography. However, these craters represent only a fraction of the impacts that have preceded them (Melosh, 1989, Soderblom et al., 2015). The craters of those preceding impacts have long since been obliterated by subsequent ballistic action, impact gardening, and seismically induced down slope movement (Richardson, 2009). However, those ancient impacts bombarded and fractured the crust to great depths, perhaps reducing much or all of the protocrust terrain to megaregolith (Zuber et al., 2013).The lunar megaregolith crust is a complex zone that probably consists of large-scale (>1 m) ejecta, impact-fractured, brecciated bedrock, melt lenses, and transported regolith. The detailed properties of the megaregolith including its thickness and distribution are essentially unknown (McKay et al., 1991). APOLLO seismic results suggest it extends down several kilometers (Figure 3.1) but recent interpretations, based on GRAIL results, suggest that the megaregolith may extend down to the mantle (Wieczorek et al., 2013) or at least to several tens of kilometers (Han et al., 2014) to a depth at which overburden pressure closes the pores.

The bulking factor B_F for rock may be defined using the equation $B_F = V/V_B - 1$ where V_B is the volume of rubble formed from breakage of a rock block of initial volume V. The bulking factor represents the % increase in the volume of a material as a result of fragmentation. On Earth, bulking factors range from 10% for granular materials like sand to as high as 80% for hard rocks, with a median of about 38% for all materials (Ofoegbu et al., 2008). Impact cratering certainly brecciates and fractures its substrate (Pilkington and Grieve, 1992; Alejano and Alonso, 2005; Collins, 2014). On the Moon, the lunar megaregolith crust is thought to have a bulk density well below the 2900 kg/m^3 grain density of its mafic protolith crust, representing a bulking factor of about 15-20%, largely due to impacts.

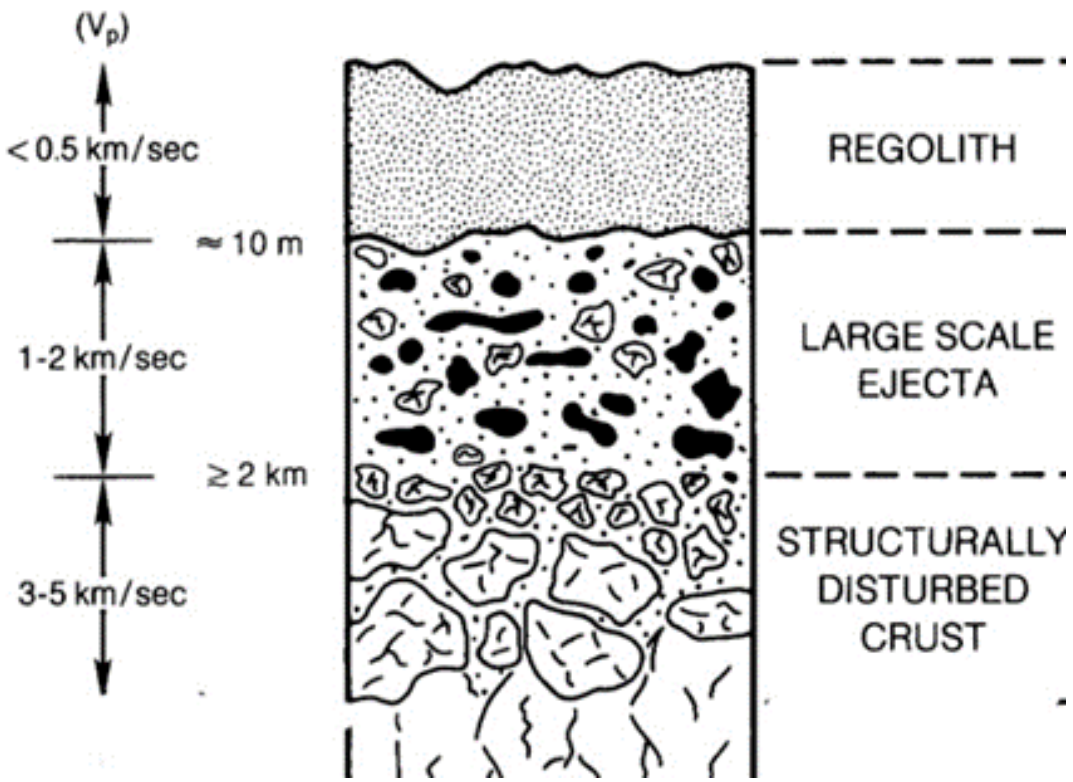

Figure 3.1. The lunar megaregolith. Lying beneath the surface regolith, the lunar megaregolith consists of fine-grained regolith from previous impact structures, ballistically transported coarse-grained ejecta, melt sheets, and brecciated bedrock (modified from Hörz et al., 1991).

Previous GRAIL studies have pointed out the possible significance to gravity interpretations of lateral heterogeneity in the bulk density of the Moon given its complex history of volcanism and impact but have not taken crater morphometry into account in their computations (Wieczorek et al., 2013; Han et al., 2014). With the exception of the currently visible craters, the cratering record of the old lunar surfaces is preserved only in the subsurface (Soderblom et al, 2015). There is little correlation or admittance left between the gravity field and surface elevation at the locations of these ancient impacts (Besserer et al., 2013). This material - the megaregolith crust - formed the target material of the impacts that resulted in the currently visible caters on the lunar highlands.

Impact structures in the lunar highlands have negative gravity anomalies compared to their surroundings (Dvorak and Phillips, 1997; Soderblom et al., 2015). The mass deficiencies extend laterally outward to the crater rim (Pilkington and Grieve, 1992; Dvorak and Phillips, 1997,

Soderblom, 2015) but their depth extent is uncertain due to the unknown density contrast between the impact structures and their surroundings. Thus, the currently visible impact structures on the lunar highlands are bulked up, compared to their protolith, the relatively older and apparently more compacted megaregolith crust. Two factors contribute to their negative density contrast: the process of crater degradation and renewed brecciation of the pre-impact crustal megaregolith.

Cratered terrain evolution models (Richardson, 2009) suggest that lunar craters are partly filled by regolith (lunar soil) that has migrated into the crater by seismically induced sliding. Based on actual Apollo measurements, the bulk density of lunar regolith is very low, no more than 1850 kg/m^3 (Mitchell et al., 1972; Carrier et al., 1972). Thick accumulations of this transported fine-grained regolith along with ballistic ejecta from nearby impacts would form lenses within the crater as the crater degrades, contributing to an overall negative density contrast between the crater structure and the surrounding megaregolith. When a crater has degraded to the point where it is no longer visible, it has lost its correlation with surface elevation and becomes part of the megaregolith crust.

The substrate of the currently visible craters is the megaregolith crust. This material has likely been compacted to some degree by the long history of small impacts on the overlying lunar surface. Such impacts may decrease the porosity of a granular protolith through heating and compaction of the target rock (Melosh, 1989; Scott and Wilson, 2005; Milbury et al., 2015). Other factors being equal, the processes of brecciation, fragmentation, and compaction by impact into the megaregolith will tend toward an average megaregolith bulk density with local fluctuations associated with freshly formed craters (Scott and Wilson, 2005; Milbury et al., 2015; Soderblom, et al., 2015). The relatively large impacts associated with the currently visible craters would have re-fragmented their target material once again, bulking the material up, and contributing to the negative density contrast between the impact structure and its surroundings.

The *GRAIL* Primary and Extended Mission (Zuber et al., 2013) resolves wavelengths as short as 18 km (Konopliv et al., 2014), a five-fold improvement on previous gravity models, making it useful for

examining anomalies associated with surface topography. Not affected by deep sources, the short wavelength data offered an opportunity to directly determine the Bouguer reduction density. The GRAIL Bouguer reduction density has been calculated by minimizing the correlation between surface topography and the resulting Bouguer anomaly. By this method, the Bouguer reduction density of the lunar highlands is 2560 kg/m^3 (Wieczorek et al., 2013). This value, has been presumed to represent the bulk density of lunar megaregolith crust, an important result used to constrain seismic, thermodynamic and petrological models of the lunar interior (Zuber et al., 2013). However, we will show that this interpretation of the Bouguer reduction density is inappropriate on the Moon where the topography is dominated by impact structures with mass deficiencies. We will show that knowledge of the distribution with elevation of the thickness of the high porosity zone associated with the currently visible craters is required to get an unbiased estimate of the bulk density of megaregolith crust from the GRAIL Bouguer reduction density.

Important constraints on lunar impact models are provided by 1185 measurements of the GRAIL residual Bouguer anomalies over complex craters in the lunar highlands (Soderblom et al., 2015). These anomalies were found to be generally negative and to scale inversely with crater diameters from 27 km to a maximum diameter $D_{MAX,}$ ranging with 95% confidence limits from 74 km to 140 km, with a best fit of 93 km. The residual Bouguer anomalies of craters larger than D_{MAX} were found to be independent of crater size, suggesting a limiting depth to impact-generated porosity.

We claim that this pronounced negative trend in the residual Bouguer anomalies over the lunar highlands can be modeled by conventional crater morphometry in conjunction with the known size-frequency distribution of complex craters. Our impact structure models consist of two homogeneous layers, one representing the megaregolith crust, the other the relatively high porosity zones associated with the currently visible craters. Constrained by the GRAIL derived Bouguer reduction density and residual Bouguer anomalies, our two-layer models show that the average bulk density of the lunar megaregolith crust in the highlands is 2225 kg/m^3. The high porosity zones associated with the currently

visible craters are bulked up in volume about 4.8 % compared to their surroundings with a density contrast of -101 kg/m^3. The thickness of the megaregolith crust is 18 km. The proportional scaling factor between the vertical extent of the high porosity zones and crater diameter is 1/6.

METHODOLOGY

The Bouguer Reduction Density

Over homogeneous crustal rock, the Bouguer anomaly is:

$$g_{BA} = g - g_{BC} = \text{random noise} \quad [1]$$

where g is the free air gravity (as processed from *GRAIL* observations onto a surface of constant elevation above the topography), and g_{BC} is the Bouguer correction for the surface topography using the Bouguer reduction density ρ_R found by minimizing the correlation between the Bouguer anomaly and topography.

However, if we consider the lunar terrain to consist of higher porosity material overlying older megaregolith, the Bouguer anomaly is equivalently represented as:

$$g_{BA} = g - g_0 - g_1 = \text{random noise} \quad [2]$$

where g_0 is the correction for the older megaregolith thickness above a deep datum using a density $\rho 0$, and g_1 is the correction for the thickness of the higher porosity material of density ρ_1.

A simple linear regression model of the higher porosity zone thickness t with surface elevation h_1 would result in a relationship of the form:

$$t = a + b\, h_1 + \text{random noise} \quad [3]$$

where a is the intercept and b is the slope, representing how the thickness of the high porosity zones change with surface elevation. The regression coefficient b is related to the correlation coefficient R between the surface elevation and the thickness of the high porosity material by:

$$b = R\, (\sigma t / \sigma h_1) \quad [4]$$

where σ represents the standard deviation. If b is zero, there is no correlation between high porosity zone thickness and topography. This would occur if *t* is either evenly or randomly distributed on the topography. In this case, the Bouguer reduction density provides an unbiased estimate of older megaregolith density. On the other hand, if b is non-zero, a correlation does exist between t and h_1. Below, we show that this lurking variable t invalidates the methodology used by Wieczorek et al. (2013) to find crustal density by simply minimizing the correlation between Bouguer gravity and surface elevation. A lurking variable is an important explanatory variable that might well escape attention in a routine statistical analysis (Joiner, 1981).

Combining [1] and [2], we see that the Bouguer correction gets contributions from both bulk densities that form the terrain:

$$g_{BC} = g_0 + g_1 \qquad [5]$$

But, using the Bouguer slab formula:

$$g_{BC} = 2\pi \gamma \rho_R h_1 \qquad [6]$$

and using the regression constants from [3], we find, ignoring terms constant with respect to h_1 :

$$g_1 = 2\pi \gamma \rho_{0\,t} = 2\pi \gamma \rho_1 b h_1 \qquad [7]$$

and:

$$g_0 = 2\pi \gamma \rho_0 (h_1 - t) = 2\pi \gamma \rho_0 (1 - b) h_1 \qquad [8]$$

Substituting [5], [6], and [7] into [3], and dividing by $2\pi \gamma h_1$, we find the Bouguer reduction density is a weighted sum of the bulk densities of the two materials that contribute to the topography (Piersol and Sprenke, 2014):

$$\rho_R = \rho_1 b + \rho_0 (1 - b) \qquad [9]$$

If, as expected, the higher porosity material is concentrated in craters, then the correlation between the thickness of higher porosity material and surface elevation is negative, as is the regression coefficient b. We further expect ρ_1 to be less than ρ_0 consistent with the mass deficiencies observed over impact craters.

The above equation places an important constraint on two-layer models of impact structures and on the interpretation of GRAIL data. The bulk density of the lunar megaregolith crust cannot be derived from a Bouguer reduction density estimated by simply minimizing the correlation between surface topography and gravity. The high porosity zones associated with the currently visible craters that form the topography must also be taken into account.

Crater Morphometry

The morphometry of craters provides constraints on numerical models for crater formation (Melosh, 1989). Lunar simple-to-complex and complex-to-basin transitions occur at crater diameters near 30 km and 200 km respectively (Melosh, 1989). The impact structures that dominate the GRAIL short period data lie within the complex crater range. Pike (1974, 1980, 1981) showed that depth d increases with diameter D, and that the d-D curve is well matched by a power law relationship of the form $d = A\ D^B$, where A and B are constants. Other aspects of fresh complex craters have also been investigated such as the morphology of the central peaks, their height and area, and how these scale with crater diameter (Wood, 1973; Wood and Head, 1976; Pike, 1977; Wood and Andersson, 1978; Hale and Head, 1979; Hale and Grieve, 1982). More recently, Kalynn (2013) has made use of Lunar Orbiter Laser Altimeter (LOLA) data and Lunar Reconnaissance Orbiter Camera (LROC) to provide improved power law relations for the central peak height and rim height above the floor for fresh complex craters.

For the models of this study, we made use of conventional power law relationships available for fresh craters on the lunar highlands: height of central peak (Kalynn et al., 2013), radius of crater floor (Pike, 1977), height of rim above floor (Kalynn et al., 2013) and apparent depth of crater below the pre-impact datum (Kalynn et al., 2013). The height of rim above pre-impact datum and thickness of ejecta outside rim is expressed by a power function of the distance scaled by the crater radius following McGetchin et al. (1973).

Because the above morphometric relations are for fresh craters, adjustments were made to account for the fact that the average complex crater still countable on the lunar surface today is not fresh. Kalynn et al. (2013) analyzed 49 relatively fresh craters on the highlands and found a best fit power law relationship $d = 1.558\ D^{0.254}$. However, we note that a power law fit through the 7 craters in her data set with the highest d/D ratios fit a parallel relationship $d = 1.84\ D^{0.254}$, suggesting that the average crater considered to be "fresh" is 15% degraded. On the other hand, a crater that is so degraded that it can no longer be counted is estimated to be 75% degraded (Richardson, 2009). Thus, it is presumed that the average complex crater visible on the lunar surface today is midway or about 45% degraded. Thus, the rim crest heights, ejecta heights, rim to floor heights and central peak to floor heights are accordingly reduced by this factor in the simulations of this study. Interpolations between the central peak elevation and the floor as well as between the rim crest and the floor are smoothly accomplished by a cosine bell function.

The subsurface morphometry of the high porosity impact zone associated with a currently visible crater is unknown and requires modeling. A parabolic shape is presumed similar to Dvorak and Phillips (1997), extending out to the rim. Although these authors suggest a maximum vertical extent T_F below the crater floor of the high porosity to extend down to 1/3 the crater rim diameter, we leave T_F as a free parameter in our models. We do, however, retain a constraint of proportional scaling between T_F and D, *for* $D<D_{MAX}$, analogous to the proportional scaling between the depth and diameter of the transient crater (Wieczorek and Phillips, 1999; Melosh and Ivanov, 1999).

For $D>D_{MAX}$, the residual Bouguer anomalies craters are independent of D (Soderblom et al., 2015), suggesting that impact-generated porosity stops at depths greater than some limiting value D_R (Soderblom et al., 2015). We use the porous zone depth below the pre-impact datum for a crater of diameter D_{MAX} to estimate D_R. The geometry of the crater structure (Figure 3.2) is therefore fixed by three parameters in our modeling: D, T_F/D, and D_{MAX}.

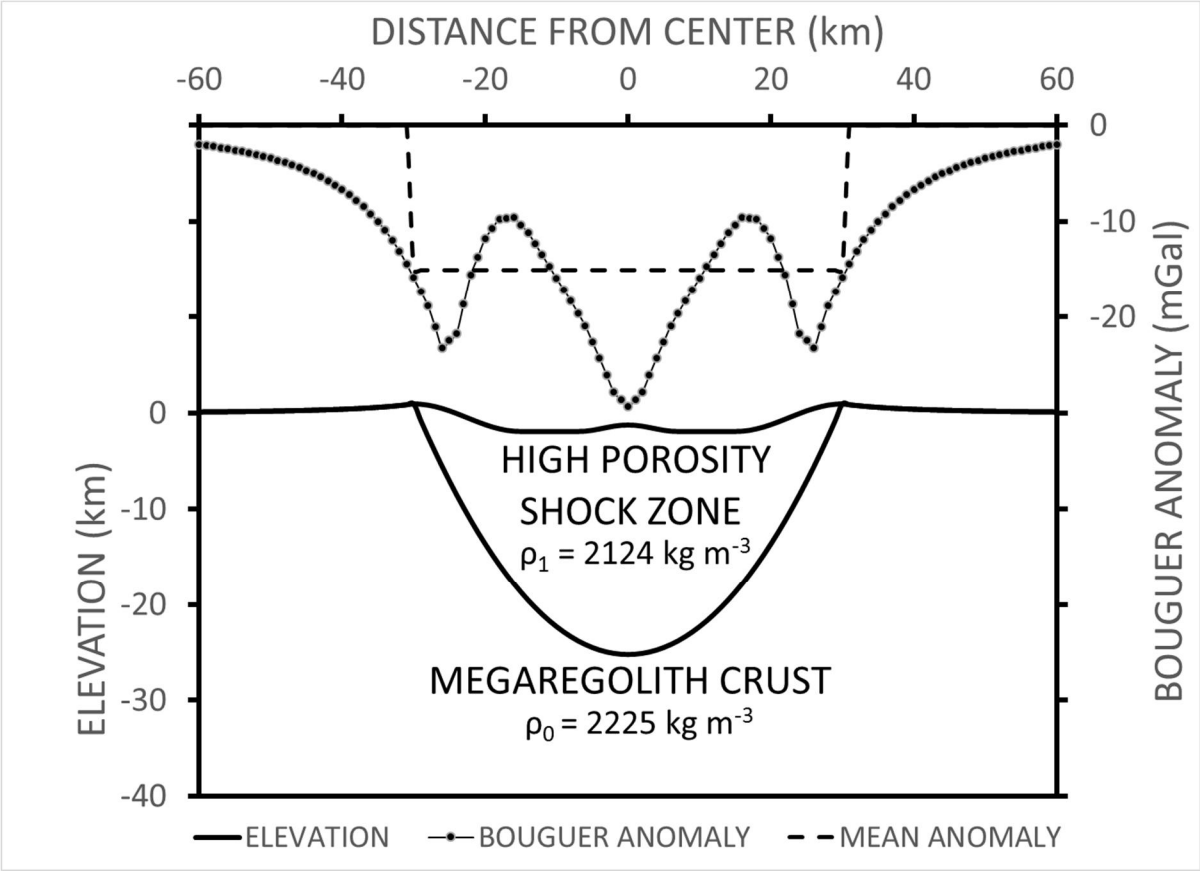

Figure 3.2. The crater morphology, Bouguer gravity, and residual Bouguer anomaly for an impact structure of diameter 60 km.

Topography of the Lunar Highlands

For any crater model based on the three parameters above, along with the size-frequency distribution for complex craters in the highlands, the regression coefficient (b) between impact zone thickness and elevation for the lunar highlands can be found if it can be assumed that the topography of the lunar highlands is formed by the currently visible (countable) complex craters.

To simulate the lunar highlands, we used complex craters with diameters in the 20-140 km range based on recent LOLA data (Smith et al., 2010; Head et al., 2010; Kadish et al., 2011.) A total of 5055 craters were included (Figure 3.3) and were distributed randomly without overlap across a simulated plane. Using the surface and sub-surface morphometry described above to estimate the surface elevation and porous zone thickness at each point, the regression coefficient b between the

thickness of the high porosity zones and surface elevation was computed using equation [9] for given model parameters T_F/D and D_{MAX}. Once b was established, equation [4] was used to establish the bulk density ρ1 of the density of the high porosity zones for a given value of megaregolith crustal density ρ0, thus insuring that our final models were consistent with the *GRAIL* Bouguer reduction density.

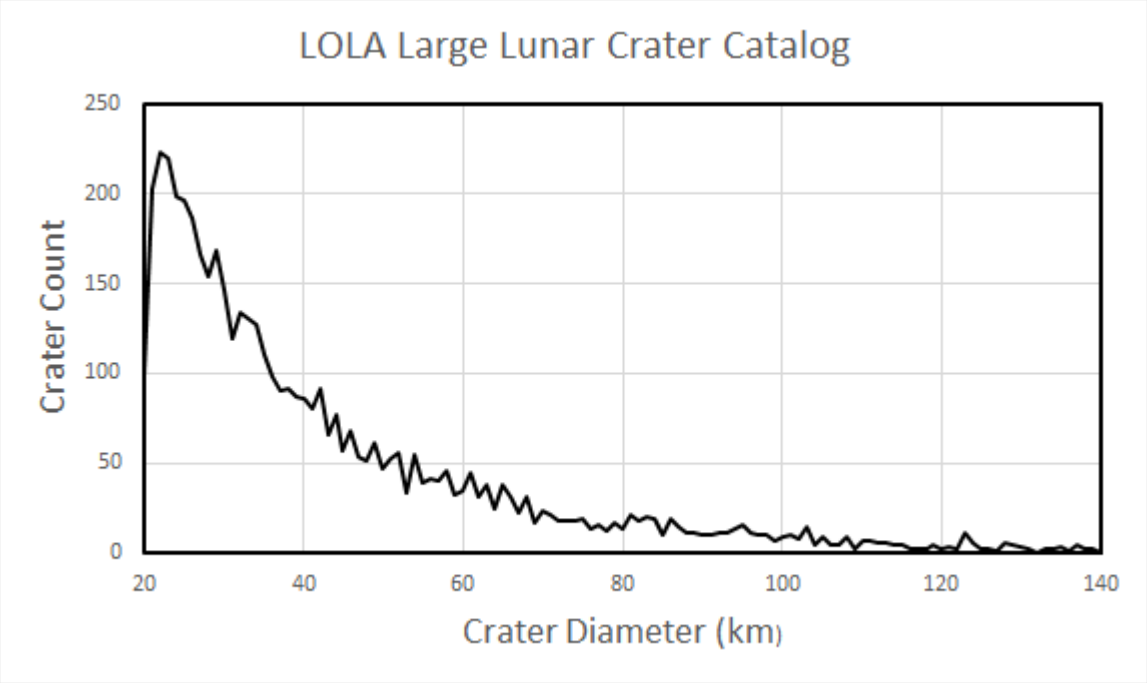

Figure 3.3. Histogram of complex crater count on the Moon (Head et al., 2010; Kadish et al., 2011).

Residual Bouguer Anomalies

Given the parameters described above, the Bouguer anomalies were then calculated for the modeled crater structures as a function of diameter *D*. To accomplish this, the 3D Talwani algorithm (Talwani and Ewing, 1960) was used, taking advantage of the circular symmetry of the surface and subsurface contours, to calculate the free-air gravity above the impact structure of given diameter. A Bouguer correction was then applied using the GRAIL Bouguer reduction density of 2560 kg/m^3 to obtain the Bouguer gravity at all distances from the center of the structure. The residual Bouguer anomaly, as defined by Soderblom et al. (2015), was then calculated as the mean Bouguer gravity of

the area within the rims divided by the Bouguer gravity at a distance equal to one crater diameter from the center. This process was repeated for craters of diameter from 27 km to D_{MAX} to match the diameter range observed by Soderblom (2015).

For each trial, the root mean square error (RMS error) in mGal was then computed between the the simulated Bouguer anomalies of our study and a best fit line through those measured by Soderblom et al. (2015). As shown in Figure 3.4, the parameters ρ0 and T_F/D are then varied until the best fit was found between the observed and simulated gravity results for the mean and 95% confidence limits of D_{MAX}. Figure 3.5 shows that the minimum RMS errors occur at well delineated values of ρ0.

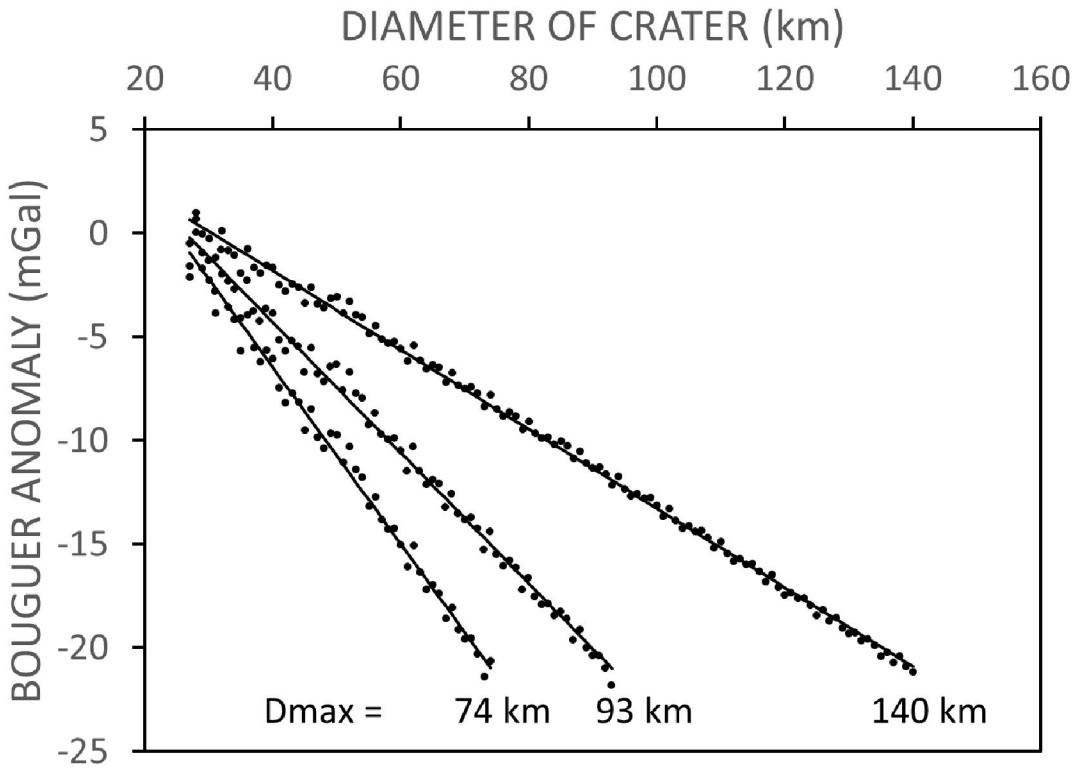

Figure 3.4. Best fit model results. The best fit matches between the residual Bouguer anomaly trends observed by Soderblom (2015) for the range of D_{MAX} values and the residual Bouguer anomalies computed by gravity modeling.

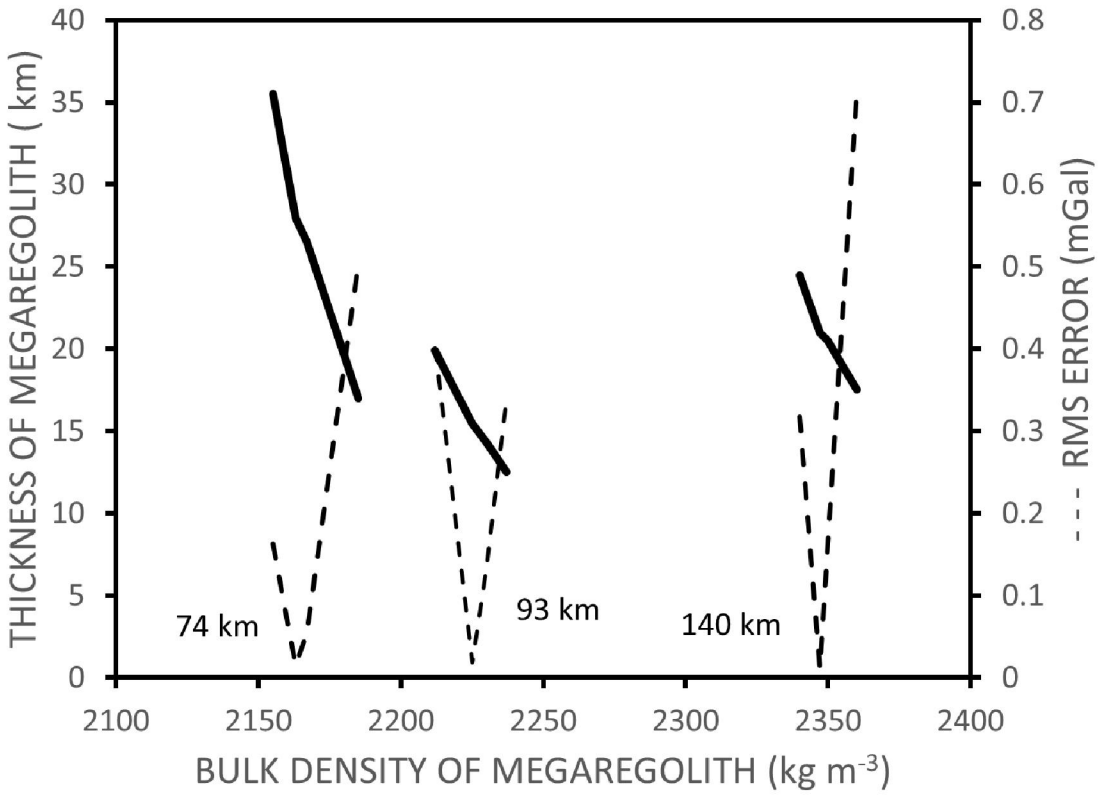

Figure 3.5. Gravity modeling results for D_{MAX} values covering the 95% confidence limits of Soderblom et al, (2015). The RMS errors minimize at the best fit values of p0 for the respective values of D_{MAX}.

D_{MAX}	ρ0	ρ1	Δρ	D_R	B	B_F	T_F/D	T_F
km	**kg m^{-3}**	**kg m^{-3}**	**kg m^{-3}**	**km**				**km**
74	2163	2105	-58	30.5	-6.80	0.028	0.30	28.0
93	2225	2124	-101	18.0	-3.31	0.048	0.167	15.5
140	2347	2281	-66	23.3	-3.22	0.029	0.226	21.0

Table 3.1. Gravity modeling results for the mean and 95% confidence limits of D_{MAX}.

RESULTS

Using conventional crater geomorphometry models in conjunction with published *GRAIL* Bouguer reduction density and residual Bouguer anomaly results, our model results (Table 3.1) show that the average bulk density of the highlands megaregolith crust is 2225 kg/m^3, 13% lower than the commonly accepted 2560 kg/m^3 value. On the average, the high porosity zones associated with the currently visible craters are bulked up 4.8 % with a density contrast of -101 kg/m^3 compared to the surrounding megaregolith crust. The proportional scaling factor between the vertical extent of the high porosity zones and crater diameter is 1/6. The overall thickness of the megaregolith crust is 18 km.

Using the 95% confidence interval (74 km – 140 km) on the D_{MAX} range found by Soderblom et al. (2015), we find a narrow range (Figure 3.6) of allowable megaregolith crustal bulk densities, 2163 to 2347 kg/m^3 as well as of high porosity zone bulk densities 2105 to 2281 kg/m^3. The density contrast ranges from -58 to -101 kg/m^3 representing bulking factors from 2.8% to 4.8%. The overall thickness of the megaregolith crust is constrained between 18 and 30.5 km.

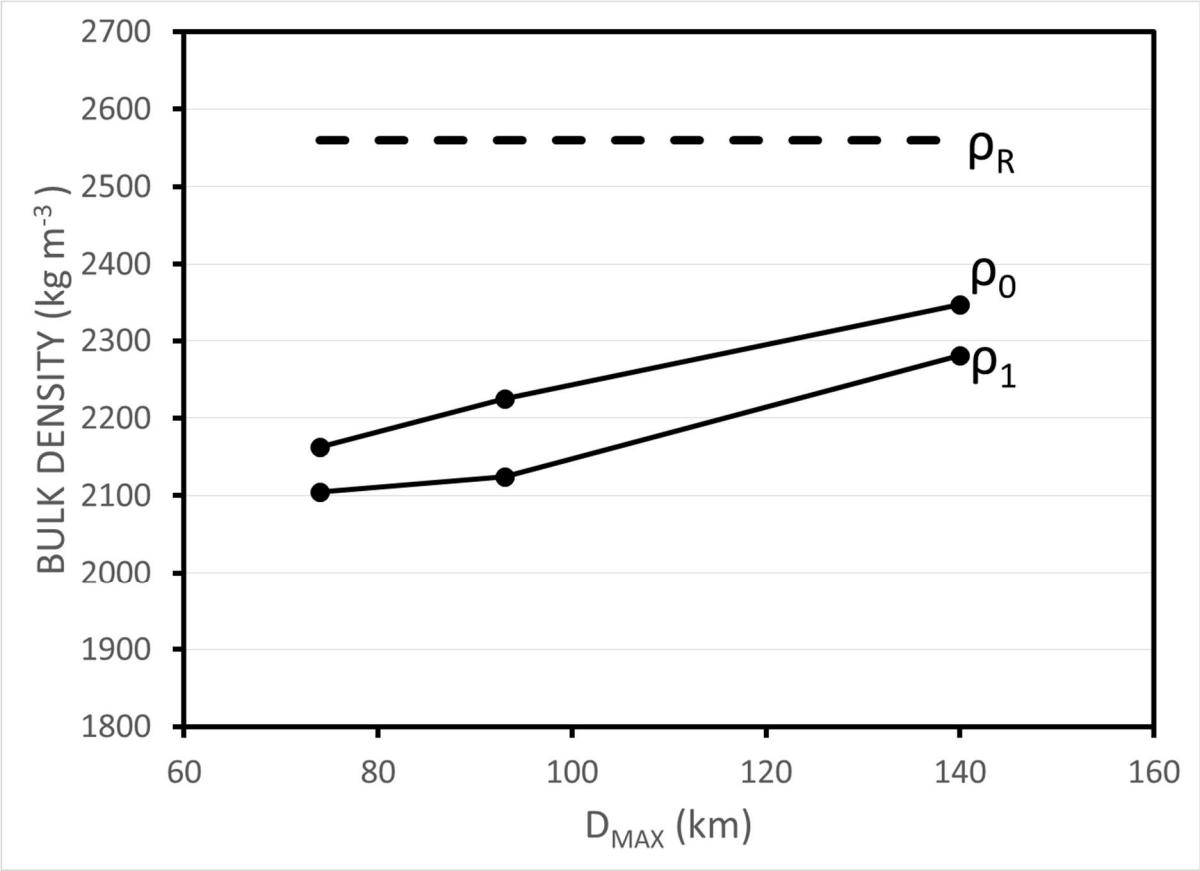

Figure 3.6. Bulk densities as a function of D_{MAX}. The bulk densities of the megaregolith crust, the high porosity zones associated with the currently visible craters, and the *GRAIL* Bouguer reduction density spanning the 95% confidence limits of D_{MAX}.

DISCUSSION

Over 98% of the GRAIL gravitational signature is associated with topography (Zuber et al., 2013). On the basis of minimizing the correlation between surface elevation and Bouguer gravity, Wieczorek et al. (2013) have asserted that the average bulk density of the fractured lunar crust (at least in the upper 3-4 km) is 2550 +/- 18 kg/m^3. However, correlation does not imply causation. The topography is not the only source of the lunar gravity field. The lurking variable present is the distribution of high porosity zones associated with the currently visible craters on the Moon. These zones being centered on the crater floors have a clear correlation with elevation. As shown by the gravity modeling results above, the Bouguer reduction density found by the minimization process provides an estimate of the

bulk density of the lunar crust that is biased 335 kg/m^3 above the actual bulk densities present in the megaregolith crust.

The models presented in this paper are in many ways similar to those Han et al. (2014) used to model the admittance of the GRAIL short period data by assuming a bulk density increase with depth (not radius) in the lunar megaregolith. Like our two-media models, their method results in a negative lateral density contrast between the visible crater structures and the surrounding uplands. Because they constrained their surface bulk densities to be near 2400 kg/m^3, Han et al. (2014) did not investigate models with densities as low as found in our study. Although we have not modeled admittance, it is evident from our two-media models that the ratio of the absolute value of the amplitude of residual gravity anomalies to surface elevation increases with crater diameter at least up to D_{MAX}. Pike (1977) showed that the depths of complex lunar craters increase as approximately the 0.3 power of *D*, slower than the proportional scaling of T_F with diameter in our models. Thus, our models involving lateral heterogeneity as a result of impact structure could provide an alternative explanation to that of Han et al. (2014) for the observed increase of gravity admittance with increasing wavelength as observed by Konopliv et al. (2014) and Lemoine et al. (2014).

The lunar surface has been mapped into separate porosity regions based on the Bouguer reduction density found for the region (Wieczorek et al., 2013). But our results show that the bulk densities (and porosities) of the megaregolith also depend on the geometry and bulk density of the high porosity zones associated with the craters in the region. The amount of impact generated porosity depends on the average size, velocity, and angles of the impacts (Soderblom et al., 2015) as well as on underlying crustal structure (Phillips et al., 2015). These factors are just as likely to vary from region to region as the regolith porosity.

The use of a biased Bouguer reduction density for the surface terrain results in complex, difficult to interpret, residual Bouguer anomalies. For example, because of over-correction, the central rims in our models produce strong negative residual Bouguer anomalies whereas the areas of the crater floor

produce relatively positive anomalies. The central peak anomalies are relatively negative for the same reason. It is interesting that Soderblom et al. (2015) report no negative tendency in their central peak residual Bouguer anomalies. We could adjust our parabolic high porosity zone in the vicinity of the central peaks to better emulate a zero central peak Bouguer anomaly. However, for the craters of importance in our study, with diameters 27 km to 93 km, the central peak areas are at or below the resolution of the GRAIL gravity, perhaps explaining the flat Soderblom measurements. Regardless, the central peak anomalies are basically irrelevant to our results because the central peak areas represent only about 4% of the rim to rim area of the crater over which the residual Bouguer anomalies are averaged to compute the residual Bouguer anomalies.

Our results are at the lower end of the 2200– 2600 kg/m^3 range of the bulk density of actual rock samples from the feldspathic highland crust (Kiefer et al., 2012). However, measurement of individual rock samples provide only an upper limit estimate of megaregolith bulk density because individual rock samples do not account for the pore space that would exist *in situ* between the rocks measured. Much lower bulk densities can be achieved by fragmentation. Apollo measurements of regolith provide the lower limit of bulk densities that might contribute material to the megaregolith. Much of the lunar megaregolith may consist of thick regolith from ancient impact structures, completely degraded by impact gardening and downslope movement of regolith by seismic-induced sliding. Based on actual Apollo measurements, the bulk density of lunar regolith is very low, no more than 1850 kg/m^3 (Mitchell et al., 1972; Carrier et al., 1972). Costes et al. (1970) gave upper bound estimates of the bulk density of regolith at two sites based on penetration resistance data from Apollo 11 and 12 landing sites; they are 1810 to 1940 kg/m^3 for Apollo 11 and 1810 to 1840 kg/m^3 for Apollo 12.

Because our modeled densities are low compared to other studies, we have studied the sensitivity of our models to various assumed parameters. These include the width of the parabola that defines the outer boundary of our high porosity zones and the degradation factor that represents the average state

of degradation of the currently visible on the lunar highlands. In the early gravity models of Dvorak and Phillips (1977) they suggest the lateral extent of the low density material be confined somewhere between the crater floor diameter and the rim to rim diameter. Our modeling suggests that the high porosity zone must indeed extend to the crater rim, as results obtained at parabola diameters only a few percent smaller than the crater diameter are unrealistic. While it is possible for the high porosity zone to extend farther than the crater rim, Dvorak and Phillips (1977) and Soderblom et al. (2015) consider it to be unlikely, as significant gravity anomalies do not extend beyond the rim.

As seen in Figure 3.7, megaregolith thickness is approximately 18 km at our best-fit D_{MAX} of 93 km using a likely 0.45 degradation factor. Even with the extreme degradation range of 0.15 to 0.75 the megaregolith thickness is well constrained between approximately 16 to 19 km. Throughout that degradation range the density contrast is approximately -105±15 kg/m^3 with the megaregolith density well below the commonly accepted value of 2560 kg/m^3.

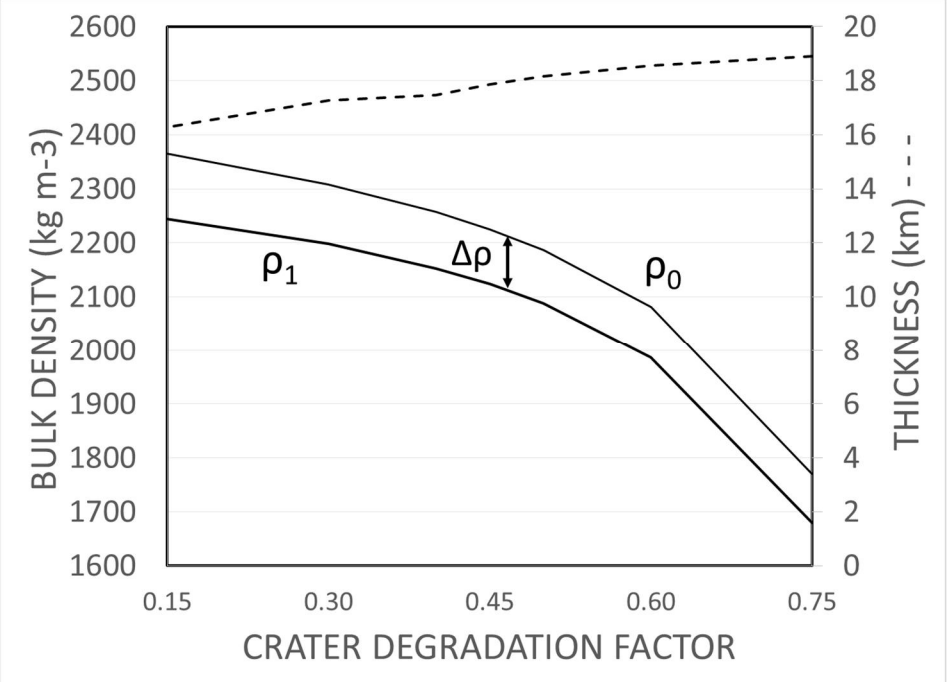

Figure 3.7. Bulk densities as a function of degradation factor. The bulk densities of the megaregolith crust and the high porosity zones associated with the craters as a function of average crater degradation factor on the highlands.

CONCLUSION

Our results here are a back-of-the-envelope calculation of the bulk density of the lunar megaregolith crust constrained by the hard work of others who have computed the Bouguer reduction density and the residual Bouguer anomalies of the currently visible craters using GRAIL data. We have made many simplifications. We use rectangular coordinates, not spherical harmonics. Our simulations simply splat the impacts without overlap on a flat plane. We assume a linear relationship between elevation and the thickness of high porosity zones associated with craters. We assume proportional scaling between crater diameters and the thickness of the high porosity zones. Instead of actually measuring the topography of the 5055 craters in our simulations, we use conventional power law morphometric relationships from the literature, some of which are not based on modern methods, to simulate the topography. Our two-layer model does not account for melt lenses and other density contrasts present in some craters; however, averaging over 5055 craters does reduce the effect such occasional, and random, density contrasts would have on our results. We presume that lateral density variations, not associated with the currently visible craters, are random and independent of elevation. The list of simplifications goes on and on. Nonetheless, it is difficult to escape the main conclusion. The currently visible craters in the lunar highlands have negative mass deficiencies, which correlate with elevation. The bulk density of the lunar megaregolith crust is much lower than the Bouguer reduction density found by minimizing the correlation between gravity and topography.

REFERENCES

Alejano, L.R., Alonso, E., 2005. Considerations of the dilatancy angle in rocks and rock masses. Int. J. Rock Mech. Min. Sci., 42 (4), 481–507, doi:10.1016/j.ijrmms.2005.01.003.

Besserer, J. et al., 2013. Theoretical and observational constraints on lunar mega-regolith thickness. Proc. Lunar Planet. Sci. Conf., 44, 2463.

Carrier III, W.D. et al., 1973. The relative density of lunar soil. Lunar Plan. Sci. Conf. Proc., 4, abstr. 2403.

Collins, G.S., 2014. Numerical simulations of impact crater formation with dilatancy. J. Geophys. Res. Planets, 119 (12), 2600–2619, doi:10.1002/2014JE004708.

Costes, N.C. et al., 1970. Apollo 11 soil mechanics investigation. Sci., 167 (3918), 739-741.

Dvorak, J., Phillips, R.J., 1977. The nature of the gravity anomalies associated with large young lunar craters. Geophys. Res. Lett., 4 (9), 380–382, doi:10.1029/GL004i009p00380

Hale, W.S., Head, J.W., 1979. Central peaks in lunar craters: morphology and morphometry. Proc. Lunar Planet. Sci. Conf., 10, 2623–2633.

Hale, W.S., Grieve, R.A.F., 1982. Volumetric analysis of complex lunar craters: Implications for basin ring formation. J. Geophys. Res., 87, A65-A76.

Han, S.C. et al., 2014. Global characteristics of porosity and density stratification within the lunar crust from GRAIL gravity and Lunar Orbiter Laser Altimeter topography data. Geophys. Res. Lett., 41 (6), 1882-1889.

Head, J.W. et al., 2010. Global distribution of large lunar craters: Implications for resurfacing and impactor populations. Sci., 329 (5998), 1504–1507, doi:10.1126/science.1195050.

Hörz, F. et al., 1991. Lunar surface processes. In Lunar Sourcebook: A User's Guide to the Moon, Heiken, G.H., Vaniman, D.T., French, B.M., eds., 61–120.

Joiner, B.L., 1981. Lurking variables: Some examples. Am. Statistician, 35 (4), 227-233.

Kadish, S.J. et al., 2011. A Global Catalog of Large Lunar Craters (≥20 km) from the Lunar Orbiter Laser Altimeter. Lunar Plan. Sci. Conf., 42, abstr. 1006.

Kalynn, J. et al., 2013. Topographic characterization of lunar complex craters. Geophys. Res. Lett., 40 (1), 38-42.

Kiefer, W.S. et al., 2012. The density and porosity of lunar rocks. Geophys. Res. Lett., 39 (7).

Konopliv, A.S. et al., 2014. High-resolution lunar gravity fields from the GRAIL Primary and Extended Missions. Geophys. Res. Lett., 41 (50), 1452–1458, doi:10.1002/2013GL059066.

Lemoine, F.G. et al., 2014. GRGM900C: A degree 900 lunar gravity model from GRAIL primary and extended mission data. Geophys. Res. Lett., 41 (10), 382–3389.

McGetchin, T.R. et al., 1973. Radial thickness variation in impact crater ejecta: Implications for lunar basin deposits. Earth Planet. Sci. Lett., 20 (2), 226-236.

McKay, D. et al., 1991. The Lunar Regolith. In Lunar Sourcebook: A User's Guide to the Moon, Heiken, G.H., Vaniman, D.T., French, B.M., eds., 286-356.

Melosh, H.J., 1989. Impact Cratering: A Geologic Process. Oxford Univ. Press (Oxford Monographs on Geology and Geophysics, No. 11), New York, 253 p.

Melosh, H.J., Ivanov, B.A., 1999. Impact crater collapse. Annu. Rev. Earth Planet. Sci., 27 (1), 385-415.

Milbury, C. et al., 2015. The effect of pre-impact porosity on the gravity signature of lunar craters. Lunar Planet. Sci., 46, abstr. 1966.

Mitchell, J.K. et al., 1972. Mechanical properties of lunar soil: Density, porosity, cohesion and angle of internal friction. Lunar Plan. Sci. Conf. Proc., 3, abstr. 3235.

Ofoegbu, G.I. et al., 2008. Bulking factor of rock for underground openings. US Nuclear Regulatory Commission, Contract NRC 02–07–006, Center for Nuclear Waste Regulatory Analyses.

Phillips, R.J. et al., 2015. Crater Bouguer anomalies probe South Pole-Aitken (SPA) basin structure, Lunar Planet. Sci. Conf., 46, abstr. 2897.

Piersol, M.W., Sprenke, K.F., 2014. Bulk Density of Lunar Highlands Bedrock from GRAIL Gravity. Lunar Plan. Sci. Conf., 45, abstr. 1006.

Pike, R.J., 1974. Depth/diameter relations of fresh lunar craters: Revision from spacecraft data. Geophys. Res. Lett., 1 (7), 291–294, doi:10.1029/GL001i007p00291.

Pike, R.J., 1977. Size-dependence in the shape of fresh impact craters on the moon, in Impact and Explosive Cratering. Roddy, D.J., Pepin, R.O., Merrill, R.B., eds., 489-509.

Pike, R.J., 1980. Control of crater morphology by gravity and target type: Mars, Earth, Moon. Proc. Lunar Planet. Sci., 11, 2159–2189.

Pike, R.J., 1981. Target-Dependence of Crater Depth on the Moon. Lunar and Planet. Sci. Conf., 12, 845–847.

Pilkington, M., Grieve, R.A.F., 1992. The geophysical signature of terrestrial impact craters. Rev. Geophys., 30 (2), 161–181, doi:10.1029/92RG00192.

Richardson, J.E., 2009. Cratering saturation and equilibrium: A new model looks at an old problem. Icarus, 204 (2), 697–715, doi:10.1016/j.icarus.2009.07.029.

Scott, E.R.D., Wilson, L., 2005. Meteoritic and other constraints on the internal structure of small asteroids. Icarus, 174 (1), 46–53, doi:10.1016/j.icarus.2004.10.014.

Smith, D.E. et al., 2010. Initial observations from the Lunar Orbiter Laser Altimeter (LOLA). Geophys. Res. Lett. 37 (18), L18204, http://dx.doi.org/10.1029/2010GL043751.

Soderblom, J.M. et al., 2015. The fractured Moon: Production and saturation of porosity in the lunar highlands from impact cratering. Geophys. Res. Lett., 42 (17), 6939-6944.

Talwani, M., Ewing, M., 1960. Rapid computation of gravitational attraction of three-dimensional bodies of arbitrary shape. Geophys., 25 (1), 203-225.

Wieczorek, M.A., Phillips, R.J., 1999. Lunar multiring basins and the cratering process. Icarus, 139 (2), 246-259.

Wieczorek, M.A. et al., 2013. The crust of the Moon as seen by GRAIL. Sci., 339 (6120), 671–675.
Wood, C.A., 1973. Moon: Central peak heights and crater origins. Icarus, 20 (4), 503-506.

Wood, C.A., Head, J.W., 1976. Comparisons of impact basins on Mercury, Mars and the Moon. Proc. Lunar Sci. Conf., 7, 3629-3651.

Wood, C.A., Andersson, L., 1978. New morphometric data for fresh lunar craters. Proc. Lunar Planet. Sci. Conf., 9, 3669–3689.

Zuber, M.T. et al., 2013. Gravity field of the Moon from the Gravity Recovery and Interior Laboratory (GRAIL) mission. Sci., 339 (6120), 668–671.